UNIVERSITY OF CALIFORNIA

Santa Barbara

Processing-Property-Performance Relationships in Solution-Processed Small Molecule Bulk Heterojunction Organic Solar Cells

A dissertation submitted in partial satisfaction of the

requirements for the degree Doctor of Philosophy

in Materials

by

Alexander Sharenko

Committee in charge:

Professor Thuc-Quyen Nguyen, Co-Chair

Professor Craig Hawker, Co-Chair

Professor Michael Chabinyc

Professor Edward Kramer

September 2014

The dissertation of Alexander Sharenko is approved.

_____

Michael Chabinyc

_____

Edward Kramer

_____

Craig Hawker, Committee Co-Chair

_____

Thuc-Quyen Nguyen, Committee Co-Chair

August 2014

Processing-Property-Performance Relationships in Solution-Processed

Small Molecule Bulk Heterojunction Organic Solar Cells

by

Alexander Sharenko

ACKNOWLEDGEMENTS

In trying to thank all those that contributed to the work contained within this document and more generally to my development as a person and professional scientist, I am incredibly humbled. I am of course indebted to my fellow Nguyen-group graduate students: Samuel Collins, Zhi Li, Jason Lin, Jack Love, Hung Phan, Chris Proctor, Niva Ran, Zach Rengert and Peter Zalar. I could not have asked for better teachers, collaborators and commiserators. I thank Drs. James Rogers and Louis Perez for their tolerance of my numerous questions on x-ray scattering and their willingness to share their expertise with me. Additionally, my time at UCSB was greatly enriched by the advice and encouragement of several UCSB post-doctoral researchers: Drs. Corey Hoven, Greg Welch, Jenny Du, Jianhua Liu and Martijn Kuik. I would like to thank Stanford Synchrotron Radiation Lightsource researchers Drs. Chad Miller, Chris Tassone, Kristin Schmidt and Alex Ayzner for their willingness to answer my questions and offer their time and advice whenever needed. I would also like to thank Dr. Mike Toney for several fruitful collaborations as well his mentorship and advice. A significant portion of the work described here would not have been possible without the contributions of my collaborators at UCSB, Drs. Tom van der Poll and Zac Henson, as well as those at the Max Planck Institute for Polymer Research, Dominik Gehrig and Dr. Frédéric Laquai. I thank the members of my committee for their insight and support during my graduate studies. Of course I would be remiss to not thank my advisor, Prof. Thuc-Quyen Nguyen, for providing me with the resources and environment that have enabled all my accomplishments over the last 4 years.

Additionally, I must thank the government and tax payers of the great country of which I was fortunate to be born a citizen. Every school I have attended from kindergarten through my PhD studies has been publically financed. I have additionally had the fortune of having my graduate studies supported by a National Science Foundation Graduate Research Fellowship. I am therefore very much a product of public investment. I am incredibly grateful for the education this investment has bestowed upon me and will be mindful of the responsibility to my country, and humanity, this gift entails as I spend my life pursuing the creation of a more prosperous, peaceful and just world through science.

My most heartfelt thanks go to my parents, Connie and Dave Sharenko, and my fellow graduate student, best friend, and girlfriend Michele Guide. Without Michele's emotional support and insightful research advice over the past 4 years I don't know that I would have completed my graduate studies, certainly not with the success or happiness that I have enjoyed. Likewise, my parents' contributions to my accomplishments to date cannot be overestimated. The sacrifices they have made on my behalf over the last 27 years are too numerous to list and the love and support they have offered too great to describe with words, so I can only offer this simplest and most inadequate of thank yous. I love you dearly.

VITA OF ALEXANDER SHARENKO

August 2014

EDUCATION

Bachelor of Science in Materials Science and Engineering, Georgia Institute of Technology, May 2010 (summa cum laude)

Doctor of Philosophy in Materials, University of California, Santa Barbara, August 2014 (expected)

REFEREED PUBLICATIONS

1. "Use of a Commercially Available Nucleating Agent to Control the Morphological Development of Solution-Processed Small Molecule Bulk Heterojunction Organic Solar Cells" A. Sharenko, N. D. Treat, J. A. Love, M. F. Toney, N. Stingelin, T.-Q. Nguyen, *J. Mater. Chem. A* **2014**
2. "The Effect of Solvent Additive on Charge Generation and Photovoltaic Performance of a Solution-Processed Small Molecule:Perylene Diimide Bulk Heterojunction Solar Cell" A. Sharenko, D. Gehrig, F. Laquai, T.-Q. Nguyen, *Chem. Mater*. **2014**
3. "Crystallization-Induced Phase Separation in Solution-Processed Small Molecule Bulk Heterojunction Organic Solar Cells," A. Sharenko, M. Kuik, M. F. Toney, T.-Q. Nguyen *Adv. Funct. Mater.* **2014***, 24,* 3543–3550.
4. "A High-Performing Solution-Processed Small Molecule:Perylene Diimide Bulk Heterojunction Solar Cell" A. Sharenko, C. Proctor, T. van der Poll, Z. Henson, T-Q Nguyen, G. C. Bazan. *Adv. Mater.* **2013**, 25, 4403–4406.
5. "Topological Considerations for the Design of Molecular Donors with Multiple Absorbing Units" L. F. Lai, J. A. Love, A. Sharenko, J. E. Coughlin, V. Gupta, S. Tretiak, T.-Q. Nguyen, A. J. Heeger, W.-Y. Wong, G. C. Bazan. *J. Am. Chem. Soc.* **2014**, *136*, 5591–5594.
6. "Increased Mobility Induced by Addition of a Lewis Acid to a Lewis Basic Conjugated Polymer," P. Zalar, M. Kuik, Z. Henson, C. Woellner, Y. Zhang, A. Sharenko, G. C. Bazan, T.-Q. Nguyen. *Adv. Mater.* **2014**, 26, 724–727.
7. "A Structure-Property-Performance Investigation of Perylenediimides as Electron Accepting Materials in Organic Solar Cells," M. Guide, S. Pla, A. Sharenko, P. Zalar, F. Fernández-Lázaro, Á. Sastre-Santos T.-Q. Nguyen. *Phys. Chem. Chem. Phys.* **2013***, 15,* 18894–18899.
8. "Film Morphology of High Efficiency Solution-Processed Small-Molecule Solar Cells" J. Love, C. Proctor, J. Liu, C. Takacs, A. Sharenko, T. van der Poll, A. J. Heeger, G. C. Bazan, T.-Q. Nguyen. *Adv. Funct. Mater.* **2013**, *23*, 5019–5026.

9. "Effects of Stereoisomerism on the Crystallization Behavior and Optoelectrical Properties of Conjugated Molecules" J. Liu, Y. Zhang, H. Phan, A. Sharenko, P. Moonsin, B. Walker, V. Promarak, T.-Q. Nguyen. *Adv. Mater.* **2013**, *25*, 3645–3650
10. "A Modular Molecular Framework for Utility in Small-Molecule Solution-Processed Organic Photovoltaic Devices" G. C. Welch, L. A. Perez, C. V. Hoven, Y. Zhang, X-D. Dang, A. Sharenko, M. F. Toney, E. J. Kramer, T.-Q. Nguyen, G. C. Bazan, *J. Mater. Chem.* **2011**, *21*, 12700.

AWARDS

2011 National Science Foundation Graduate Research Fellowship

ABSTRACT

Photovoltaic devices that directly convert sunlight to electrical power have the potential to generate terawatts of usable power if they can be produced economically at scale. Solution-processed bulk heterojunction organic photovoltaics (BHJ OPVs) are a particularly interesting photovoltaic technology primarily because they have demonstrated power conversion efficiencies (PCEs) exceeding 10% and can be solution-processed over large areas, indicating their potential as a cost-effective, scalable source of renewable energy. Whereas BHJ OPVs utilizing polymer donors and functionalized fullerene acceptors dominate the organic solar cell literature, BHJ OPVs have recently been fabricated using small molecule donors with PCEs on par with their polymeric counterparts. The work comprising this dissertation therefore consists of two separate but related goals: 1) understanding and controlling the crystallization of small molecule donor materials in BHJ blends with functionalized fullerene acceptors and 2) identifying the efficiency limiting processes of organic solar cells utilizing perylene diimide (a commercial dye) acceptor molecules and small molecule donor materials.

It is well established that the specifics of the bulk heterojunction morphology (phase separation, crystallinity, etc.) profoundly affect BHJ OPV device PCE. Controlling the BHJ morphology is thus of great importance. Using in-situ thermal annealing grazing incidence wide and small angle x-ray scattering it was discovered that the driving force for phase separation in BHJ OPV systems utilizing small molecule donor materials and functionalized fullerene acceptors is the crystallization of the small molecule donor material. Additionally, it was shown that this crystallization process, and therefore the development of the bulk

heterojunction morphology and device performance, can be controlled by using commercially available nucleating agents designed for the clarifying of isotactic polypropylene.

Functionalized fullerene acceptors, ubiquitous in high efficiency BHJ OPVs, are produced via particularly solvent and energy intensive techniques and exhibit small extinction coefficients across the terrestrial solar spectrum. There then exists obvious benefits for using inexpensive, easily mass-produced fullerene alternatives that strongly absorb solar photons. Perylene diimides (PDIs) are a class of organic dye molecules with high electron affinity similar to fullerenes, large extinction coefficients across the terrestrial solar spectrum and relatively high electron mobilities, thus making them attractive for use as electron acceptors in organic solar cells. A BHJ OPV with a PCE of 3.1% was fabricated using a small molecule donor material and a PDI acceptor, making this one of the most efficient BHJ OPV devices utilizing a non-fullerene acceptor. Use of the solvent additive 1,8-diiodooctane (DIO) was shown to greatly improve the PCE of these devices. Using UV-Vis and transient absorption pump-probe experiments it was shown that use of DIO increases the structural order of both the donor and acceptor molecule, corresponding to a drastic increase in the efficiency with which excited states separate into free charge carriers and therefore largely explaining the drastic increase in solar cell figures of merit when using the solvent additive.

TABLE OF CONTENTS

Section II: Investigatoin of the Morphological, Optical and Electronic Properties of a Solution-Processed Small Molecule Bulk Heterojuntion Organic Solar Cell Utilizing a Perylene Diimide Acceptor

Introduction

A. Motivation for Work

The world is in need of economically viable, low-carbon sources of energy on a terawatt scale in order to mitigate the potentially devastating consequences of anthropogenic climate change.[1,2] As the sun directly provides several times the total energy demand of human civilization on a daily basis, solar energy production has the potential to offset more carbon-intensive energy production from fossil fuel-based technologies.[3–5] Solar energy can be converted to useful energy in any one of several ways. Photovoltaic devices are those that directly convert solar photons to electrical power, usually via the use of solid state semiconducting materials. Additionally, photovoltaic devices produce no direct emissions. Photovoltaic devices therefore have the potential to serve as a large scale, low-carbon source of energy. Widespread adoption of photovoltaic technology, however, has been hindered by the relatively high cost of energy produced from the photovoltaic effect.

The high cost of photovoltaic energy is in part the result of the large amount of energy required for the processing of the silicon[6] found in the majority of commercial solar panels as well as the rare and/or toxic materials used in newer thin film photovoltaic materials such as cadmium telluride and copper indium gallium selenide. Organic photovoltaic (OPV) devices have the potential to overcome these obstacles as they are synthesized from readily available petroleum feedstock materials and can be processed using large area, high throughput solution deposition technologies such roll-to-roll coating.[7–9] OPVs have the additional benefit of being mechanically flexible, allowing the possibility of solar cells that can be rolled or folded for ease of storage and transportation. They also possess high extinction coefficients making it possible for very thin films (~300 nm) to

absorb almost all incident light. Their optical band gaps are also highly modular based on their chemical structure meaning their color can be tuned based on aesthetic or architectural desires.[10] OPVs devices then have the potential to serve as a large area source of clean energy and/or could be used in niche applications that require bendability or a specific color scheme.

B. Solar Cell Figures of Merit

Solar cells are evaluated by applying a voltage and measuring the current response of the device while irradiating with a light source. This produces a current density-voltage (*J-V*) curve (Figure 1). The solar cell figures of merit are then extracted from this *J-V* curve. The short-circuit current density (J_{SC}) is the current density from the device at zero applied voltage. The open-circuit voltage (V_{OC}) is the voltage at which the current density from the device is zero. The max power point is the point on the curve where the power, that is the product of current and voltage, is maximized (Figure 1). The fill factor (FF) is then defined as:

$$FF = \frac{\max\ power\ point}{V_{OC}\, J_{SC}} \quad (1)$$

Perhaps the figure of merit of greatest importance, however, is the power conversion efficiency (PCE). The PCE is a measure of how efficiently a photovoltaic device converts solar energy into electrical energy. PCE is calculated as follows:

$$PCE = \frac{FF\, V_{OC}\, J_{SC}}{P_{in}} \quad (2)$$

Where P_{in} stands for the incident power. Under standard Air Mass 1.5 Global (AM 1.5 G) testing conditions P_{in} is defined as 100 watts/cm^2.[11]

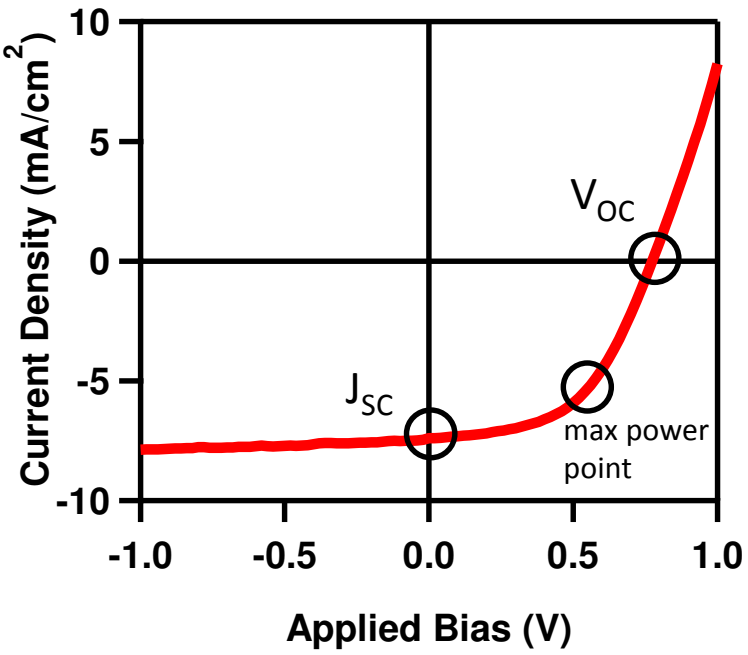

Figure 1: Typical *J-V* curve for a photovoltaic device.

Another important solar cell figure of merit is the quantum efficiency of the device. This figure of merit is an indicator of how efficiently a solar cell converts photons into electrical current and is typically expressed as a percentage. The quantum efficiency can be further broken down into the percentage of incident photons converted into electrical current, i.e. the external quantum efficiency (EQE), and the percentage of absorbed photons converted into electrical current, i.e. the internal quantum efficiency (IQE).

When the EQE spectrum of a device is integrated, it should yield a current density value equivalent to that of the device's J_{SC}. This check should be routinely performed to confirm J_{SC} values determined from *J-V* curves, which are subject to some error given the difficulty associated with accurately measuring a device area. For an efficient device, a significant difference between integrated EQE and J_{SC} is usually an indication of unacceptable experimental error.[12,13] Additionally, when calculating the IQE, care must be taken to

account for photons parasitically absorbed by the electrodes and interlayers of the device as well as optical interference effects.[14] Failure to appropriately account for these optical effects can lead to erroneous conclusions about device operation.[15,16] More detailed information on how to accurately test excitonic solar cells can be found elsewhere.[17]

C. Bulk Heterojunction Organic Solar Cell Operating Principles

The inorganic semiconductors that the majority of commercial solar cells are made of directly produce free charge carriers, i.e. a spatially separated electron and hole, upon absorption of a photon. These free charge carriers additionally have relatively long (~100 μm) diffusion lengths. These characteristics then enable the fabrication of efficient inorganic solar cells using relatively simple p-n or p-i-n junction architectures. Organic semiconductors, however, have low dielectric constants (~2-3) and the coulombic interaction between the hole and electron generated by absorption of a photon is therefore not sufficiently screened to allow for spontaneous spatial separation. In an organic semiconductor, absorption of a photon thus produces a bound electron-hole pair known as an exciton. The diffusion length of an exciton is additionally typically limited to ~10 nm in a solution-processed organic semiconductor.[18]

The formation of an exciton rather than spatially separated charge carriers upon photon absorption in an organic semiconductor as well as this exciton's relatively short diffusion length profoundly influences the architecture required for the fabrication of high efficiency organic solar cells. In order to overcome the coulombic interaction between the electron-hole pair within the exciton a type II molecular heterojunction between an electron donating molecule and an electron accepting molecule must be formed.[19] This interface provides a driving force for a photoexcited, bound electron located on the electron donating molecule's

lowest unoccupied molecular orbital (LUMO) to charge transfer to the LUMO of the electron accepting molecule, thus generating an unbound electron on the electron accepting molecule. Likewise, hole transfer from the electron acceptor's highest occupied molecular orbital (HOMO) to the electron donator's HOMO proceeds in similar fashion to produce an unbound hole on the electron donating molecule. This exciton splitting process is sometimes known to proceed via an intermediate charge transfer state (CT state) where charge transfer between electron donor and acceptor has occurred, but the coulombic interaction between the electron on the acceptor and the hole on the donor has not yet been overcome.

In practice excitons can be split and an organic solar cell fabricated by forming a bilayer organic solar cell consisting of a layer of electron donating molecule on top of a layer of electron accepting molecule sandwiched between electrodes of opposite polarity (Figure 2).[20] In order to ensure generated excitons are able to diffuse to the donor-acceptor interface to be split into free charge carriers, the donor and acceptor layers can roughly only be made as thick as the exciton diffusion length. These very thin layers unfortunately only absorb a fraction of incident light. The J_{SC}, and in turn the PCE, of these devices is then severely limited by the short diffusion length of an exciton in an organic solar cell utilizing a bilayer architecture.

The shortcomings of the bilayer architecture were overcome with the development of the bulk heterojunction (BHJ) architecture (Figure 2).[21] A BHJ consists of nanoscale interpenetrating and bicontinuous domains of electron donating and electron accepting molecules. The interpenetrating nature of this morphology provides vastly more donor-acceptor interfacial area compared to a bilayer architecture and thus increases the probability that an exciton will reach such an interface to be split into a free electron and hole before

decaying back to the ground state. The bicontinuous nature of the BHJ morphology then allows generated electrons (holes) to traverse through the acceptor (donor) phase to be collected at the cathode (anode). A BHJ morphology therefore increases the PCE of OPV devices compared to bilayers by increasing the donor-acceptor interfacial area that is necessary to convert generated excitons to free charge carriers, thereby allowing for a thicker organic semiconductor layer which increases the amount of incident light absorbed.

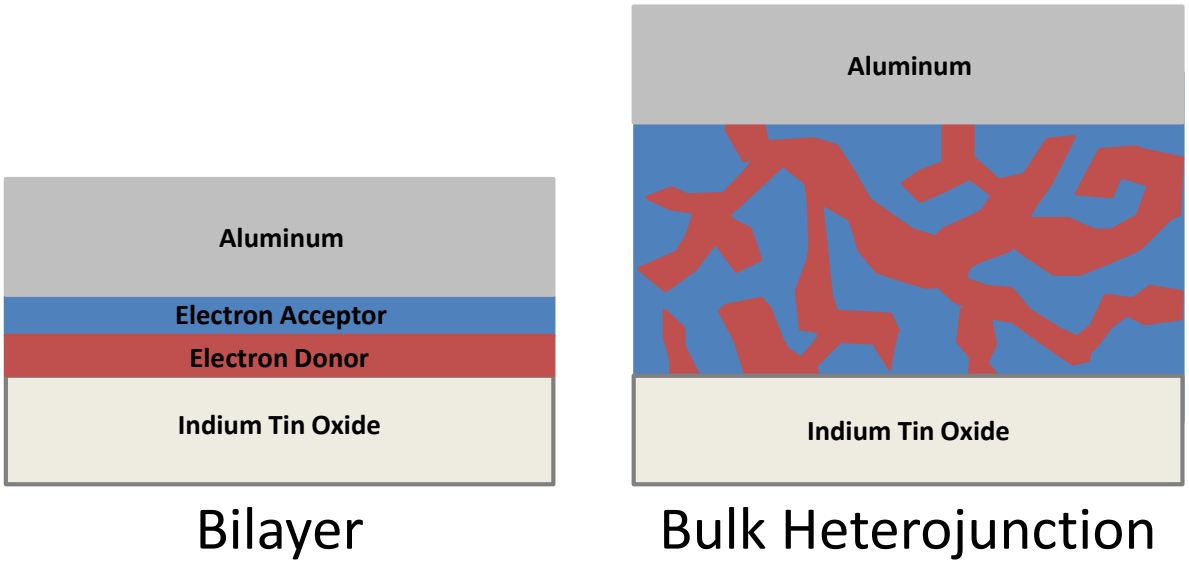

Figure 2: Cartoon schematics of a bilayer and bulk heterojunction organic solar cell architecture.

For a BHJ OPV device to generate electrical power absorbed photons must be converted to excitons, which must then be split to produce free charge carriers and then these free charge carriers must be successfully collected at the appropriate electrode. These processes are illustrated schematically in Figure 3. There are numerous possibilities for competing and deleterious processes to disrupt this power generating scheme. The active layer may not be thick enough to absorb all incident photons or the donor and/or acceptor domains may be larger than the exciton diffusion length, thus reducing the potential J_{SC}. Excitons may form

CT states that do not further dissociate into free charge carriers for reasons that are still vigorously debated.[22,23] Free charge carriers may recombine because of low mobilities or a lack of a continuous transport pathway to an electrode. Recombination is generally classified as either geminate, those processes involving an electron-hole pair produced from a single photon absorption, or nongeminate, those processes involving spatially separated free electrons and holes. Several excellent reviews discuss these processes in more detail.[24–26] Given that a BHJ OPV device requires the formation of a relatively specific and complicated morphology that is then fraught with possible loss mechanisms, it is perhaps surprising that BHJ OPV devices work at all! BHJ OPV devices with IQEs approaching 100% and PCEs of approximately 8% have, however, been fabricated.[22,27,28]

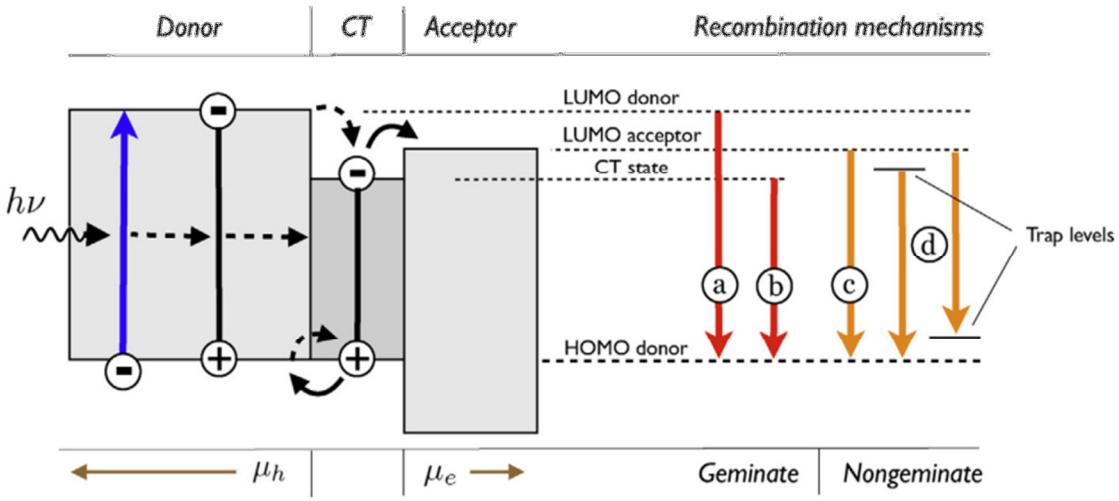

Figure 3: Left: From left to right. Incoming light is absorbed in the donor material (blue arrow); a bound exciton is formed. The exciton diffuses toward the donor–acceptor interface. The exciton transfers onto the interface state i.e. CT state (dashed arrows), after which the exciton dissociates (solid arrows) and the free hole and electron drift through the donor and acceptor phase respectively, to the extracting contacts (brown arrows). Right: An overview of the four most encountered recombination mechanisms. The geminate mechanisms: (a) exciton decay after excitation, (b) recombination through the CT state, and the nongeminate mechanisms: (c) recombination of free holes and electrons, (d) recombination of free carrier with carrier trapped on sites within the band gap. Reprinted with permission from Elsevier from reference 25.

D. Bulk Heterojunction Processing and Morphological Characterization

From the above it is clear that the morphology of a BHJ OPV device profoundly influences its solar cell figures of merit. It is therefore imperative that processing techniques exist to control BHJ morphology as well as characterization techniques that allow the BHJ morphology to be probed and quantified. The BHJ morphology is commonly manipulated by modulating the donor-acceptor blend ratio[29,30], the casting solvent or the incorporation of solvent additives into the casting solution[27,31] as well as post film formation thermal annealing.[27,32] These processing techniques generally allow the manipulation of the solid state order (crystallinity)[27,32–34] and spatial distribution (phase separation)[34,35] of the donor and acceptor molecules within the BHJ. These specific aspects of the BHJ morphology must then be characterized so processing-property-performance relationships can be established. Solid state order is generally probed using grazing incidence wide angle x-ray scattering (GIWAXS), transmission electron microscopy (TEM) or UV-Vis absorption spectroscopy. The spatial distribution of donor and acceptor are often characterized using TEM, grazing incidence small angle x-ray scattering (GISAXS), or resonant soft x-ray scattering. This is of course not a comprehensive list of techniques used for BHJ characterization. Several excellent reviews offer a more thorough discussion of this topic.[36–39]

Briefly, GIWAXS and GISAXS will be discussed in further detail because of their importance to the work contained within this dissertation. GIWAXS and GISAXS are complimentary x-ray scattering techniques in the context of BHJ characterization in that GIWAXS is used to provide information on structural order whereas GISAXS is used to provide information on phase separation.[40] As x-ray scattering techniques, they offer the additional advantage over microscopy techniques such as atomic force microscopy or TEM

in that they probe a much larger sample volume so that interpretations of GIWAXS or GISAXS data are representative of the dominant morphological features in a sample.

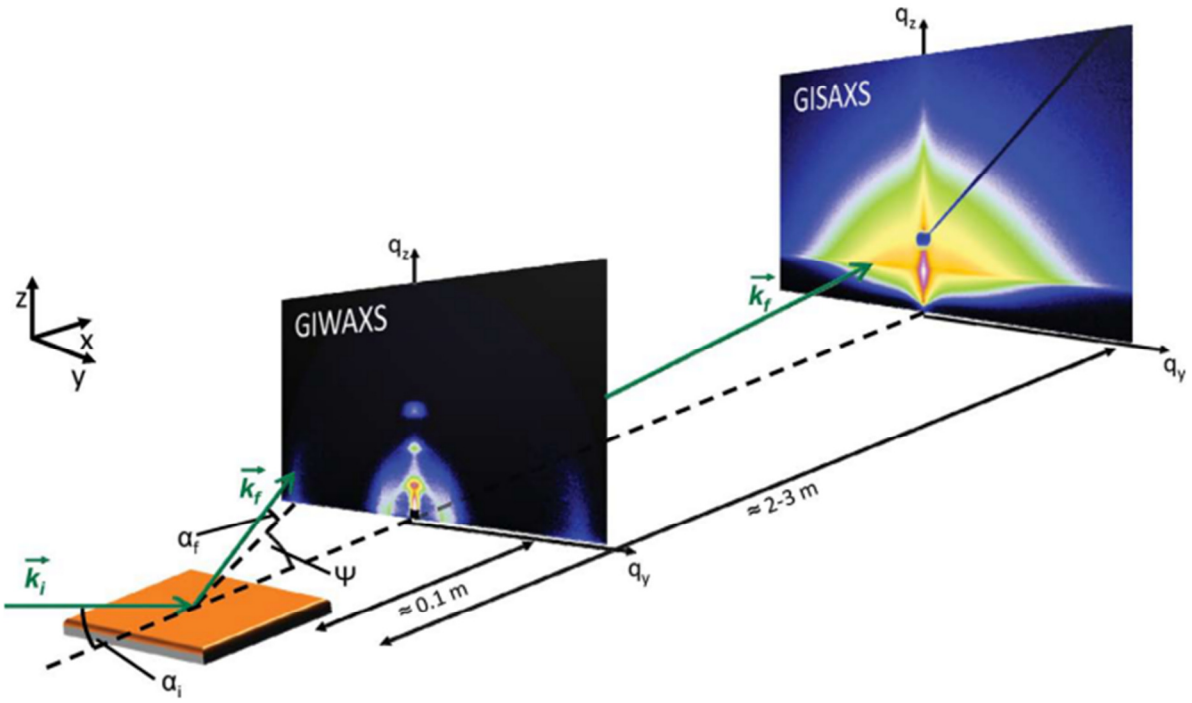

Figure 4: Typical experimental set up of GIWAXS and GISAXS. α denotes the incident angle (on the order of 0.1˚). Reprinted with permission from reference 39. © 2014 WILEY-VCH Verlag GmbH & Co. KGaA, Weinheim.

1. GIWAXS

GIWAXS is an x-ray diffraction technique and is therefore sensitive to probing crystalline order within a film.[40,41] The grazing incidence geometry allows for the creation of an evanescent wave within the film. This evanescent electric field increases the scattered intensity from the film, which is important when trying to probe thin, relatively disordered, carbonaceous materials such as organic semiconductors. The distribution of this evanescent electric field within the film can additionally be tuned to ensure scattering is dominated by the BHJ film rather than the substrate[33] and to allow for depth profiling of specific ordered

features as function of depth within the BHJ.[42] When GIWAXS is combined with an area detector, crystallites distributed over all polar angles within the film are able to be probed rather than just those with their scattering vector parallel to the diffracted plane normal as in a traditional specular scan. This allows for the straightforward determination of any crystalline texture. The combination of a planar area detector and a grazing incidence geometry, however, does not allow for the probing of crystallites within a few degrees of those directly out of plane because of how the orientation and Ewald spheres overlap.[43] This leads to a "missing wedge" of crystallites directly out of plane. Additionally, the grazing incidence geometry is particularly amenable to in-situ studies as it does not require thin films to be removed from their substrate and minimizes exposure times because of the increased scattered intensity from the standing wave formed within the film.

GIWAXS can also be used to quantify the crystalline order within a film. This is most commonly done by calculating the crystalline correlation length (CCL) of a material. The CCL is calculated from the broadening of diffraction peaks:

$$CCL = \frac{2\pi}{FWHM} \quad (3)$$

Where the FWHM is the full width at half maximum of a given peak. Peak broadening occurs because of finite sized crystallites, crystalline disorder and instrumentation effects. In organic semiconductors, especially when using synchrotron x-ray facilities as is common practice, instrumentation effects are dominated by the effect of finite sized crystallites and crystalline disorder. In systems with multiple orders of a single diffraction peak, it is relatively straightforward to deconvolute the effects of crystallite size vs. disorder on peak broadening with the Warren-Averbach analysis.[39] This, however, is rarely the case for organic semiconductors. Accordingly, the CCL is interpreted as having contributions from

crystallite size and disorder effects in organic semiconductors and can be thought of as the spatial distribution over which crystalline order is maintained within a material.[44] The CCL is rarely greater than 25 nm for most solution processed organic semiconductors.

Using GIWAXS to calculate the degree of crystallinity of a material is more difficult. The diffracted intensity from different GIWAXS samples cannot be compared to determine their relative structural order because the diffracted intensity from GIWAXS is highly sensitive to the incident angle and resulting evanescent electric field within a sample, which will undoubtedly vary from sample to sample because of the limitations of the motors and optics of the experimental set-up. Traditionally, the degree of crystallinity in organic polymers has been calculated with x-ray scattering by comparing the intensity of the diffraction from ordered regions of the polymer to the scattering arising from amorphous regions of the polymer.[45] Using this method it is then possible to compare the degree of crystallinity for example of identical polyethylene samples processed different ways. This method has been adapted for organic semiconductors[33], but is complicated when analyzing a sample comprising a blend of multiple materials or a more crystalline sample where it is difficult to accurately define the scattering associated with amorphous regions of the material. A relatively new method has been developed to use GIWAXS to calculate a relative degree of crystallinity between samples, however, it requires use of two separate synchrotron beam lines and so is not extremely practical.[46] These techniques to calculate the degree of crystallinity are limited to comparing the same material because of structure factor considerations and cannot determine crystallinity on an absolute scale.

2. GISAXS

GISAXS additionally has many of the advantages of GIWAXS in that the same grazing incidence geometry allows for increased scattering from the BHJ layer and is amenable to in-situ studies. In practice, the only difference between GIWAXS and GISAXS is the sample to detector distance. In GISAXS, the detector is usually 1-3 meters from the sample whereas in GIWAXS the detector is usually less than a meter from the sample. The sample to detector distance determines the q range being probed. The scattering vector, q, can be related to real space, d, in the following manner:

$$q = \frac{2\pi}{d} \quad (4)$$

GISAXS is then sensitive to probing features on the order of 10 nm to 1 μm. Scattering contrast in GISAXS is generated by electron density inhomogeneities, for example between donor-rich and acceptor-rich phases in a BHJ blend. GISAXS is therefore well suited to probing blend phase separation in BHJ OPV films.[40] In highly ordered organic systems such as block copolymers, GISAXS is capable of providing detailed structural information, such as the lattice the different domains occupy.[47] In less ordered systems, extracting quantitative information from GISAXS profiles requires fitting experimental data to a model[48,49], however, modeling a BHJ OPV blend is extremely challenging given the irregularly shaped, polydisperse, interconnected and randomly distributed domains characteristic of a BHJ morphology. Due to these complexities there exists no widely accepted GISAXS model for BHJ OPV blends and therefore GISAXS data on BHJ blends is most often interpreted qualitatively or only semi-quantitatively. When probing a BHJ blend, to a first order approximation, films will produce a peak or shoulder in scattered intensity at a q value corresponding to the average length scale associated with the differences in electron density,

i.e. the length scale of phase separation. Additionally, the intensity of this peak or shoulder within a given sample undergoing a series of in-situ measurements is proportional to the extent of blend phase separation. More information on GISAXS can be found in several excellent reviews.[50,51]

E. References

1. Huber, M. & Knutti, R. Anthropogenic and natural warming inferred from changes in Earth's energy balance. *Nat. Geosci.* **5,** 31–36 (2012).
2. Peters, G. P. *et al.* The challenge to keep global warming below 2 °C. *Nat. Clim. Change* **3,** 4–6 (2013).
3. Blankenship, R. E. *et al.* Comparing Photosynthetic and Photovoltaic Efficiencies and Recognizing the Potential for Improvement. *Science* **332,** 805–809 (2011).
4. Quaschning, V. *Understanding Renewable Energy Systems*. **1,** (Earthscan, 2005).
5. Smith, Z. & Taylor, K. *Renewable and Alternative Energy Resources: A Reference Handbook*. (ABO-CLIO, Inc., 2008).
6. Knapp, K. & Jester, T. Empirical investigation of the energy payback time for photovoltaic modules. *Sol. Energy* **71,** 165–172 (2001).
7. Krebs, F. C., Espinosa, N., Hösel, M., Søndergaard, R. R. & Jørgensen, M. 25th Anniversary Article: Rise to Power – OPV-Based Solar Parks. *Adv. Mater.* **26,** 29–39 (2014).
8. Krebs, F. C., Gevorgyan, S. A. & Alstrup, J. A roll-to-roll process to flexible polymer solar cells: model studies, manufacture and operational stability studies. *J. Mater. Chem.* **19,** 5442–5451 (2009).

9. Andersen, T. R. *et al.* Scalable, ambient atmosphere roll-to-roll manufacture of encapsulated large area, flexible organic tandem solar cell modules. *Energy Environ. Sci.* (2014). doi:10.1039/C4EE01223B
10. Kroon, R., Lenes, M., Hummelen, J. C., Blom, P. W. M. & de Boer, B. Small Bandgap Polymers for Organic Solar Cells (Polymer Material Development in the Last 5 Years). *Polym. Rev.* **48,** 531–582 (2008).
11. Oriel Product Training: Solar Simulation. at <http://assets.newport.com/webDocuments-EN/images/12298.pdf>
12. Lee, J. *et al.* High-Efficiency Panchromatic Hybrid Schottky Solar Cells. *Adv. Mater.* **25,** 256–260 (2013).
13. Potscavage, W. J. Comment on High-Efficiency Panchromatic Hybrid Schottky Solar Cells. *Adv. Mater.* **25,** 4825–4825 (2013).
14. Burkhard, G. F., Hoke, E. T. & McGehee, M. D. Accounting for Interference, Scattering, and Electrode Absorption to Make Accurate Internal Quantum Efficiency Measurements in Organic and Other Thin Solar Cells. *Adv. Mater.* **22,** 3293–3297 (2010).
15. Grancini, G. *et al.* Hot exciton dissociation in polymer solar cells. *Nat. Mater.* **12,** 29–33 (2013).
16. Scharber, M. Measuring internal quantum efficiency to demonstrate hot exciton dissociation. *Nat. Mater.* **12,** 594–594 (2013).
17. Snaith, H. J. How should you measure your excitonic solar cells? *Energy Environ. Sci.* **5,** 6513–6520 (2012).

18. Lin, J. D. A. *et al.* Systematic study of exciton diffusion length in organic semiconductors by six experimental methods. *Mater. Horiz.* **1,** 280–285 (2014).
19. Sariciftci, N. S., Smilowitz, L., Heeger, A. J. & Wudl, F. Photoinduced Electron Transfer from a Conducting Polymer to Buckminsterfullerene. *Science* **258,** 1474–1476 (1992).
20. Tang, C. W. Two-layer organic photovoltaic cell. *Appl. Phys. Lett.* **48,** 183–185 (1986).
21. Yu, G., Gao, J., Hummelen, J. C., Wudl, F. & Heeger, A. J. Polymer Photovoltaic Cells: Enhanced Efficiencies via a Network of Internal Donor-Acceptor Heterojunctions. *Science* **270,** 1789–1791 (1995).
22. Vandewal, K. *et al.* Efficient charge generation by relaxed charge-transfer states at organic interfaces. *Nat. Mater.* **13,** 63–68 (2014).
23. Bakulin, A. A. *et al.* The Role of Driving Energy and Delocalized States for Charge Separation in Organic Semiconductors. *Science* **335,** 1340–1344 (2012).
24. Lakhwani, G., Rao, A. & Friend, R. H. Bimolecular Recombination in Organic Photovoltaics. *Annu. Rev. Phys. Chem.* **65,** 557–581 (2014).
25. Dimitrov, S. D. & Durrant, J. R. Materials Design Considerations for Charge Generation in Organic Solar Cells. *Chem. Mater.* DOI: 10.1021/cm402403z (2013). doi:10.1021/cm402403z
26. Proctor, C. M., Kuik, M. & Nguyen, T.-Q. Charge Carrier Recombination in Organic Solar Cells. *Prog. Polym. Sci.* **38,** 1941–1960 (2013).
27. Love, J. *et al.* Film Morphology of High Efficiency Solution-Processed Small-Molecule Solar Cells. *Adv. Funct. Mater.* **23,** 5019–5026 (2013).

28. Bartelt, J. A. *et al.* The Importance of Fullerene Percolation in the Mixed Regions of Polymer–Fullerene Bulk Heterojunction Solar Cells. *Adv. Energy Mater.* **3,** 364–374 (2012).

29. Welch, G. C. *et al.* A modular molecular framework for utility in small-molecule solution-processed organic photovoltaic devices. *J. Mater. Chem.* **21,** 12700 (2011).

30. Walker, B. *et al.* Nanoscale Phase Separation and High Photovoltaic Efficiency in Solution-Processed, Small-Molecule Bulk Heterojunction Solar Cells. *Adv. Funct. Mater.* **19,** 3063–3069 (2009).

31. Peet, J. *et al.* Efficiency enhancement in low-bandgap polymer solar cells by processing with alkane dithiols. *Nat. Mater.* **6,** 497–500 (2007).

32. Verploegen, E. *et al.* Effects of Thermal Annealing Upon the Morphology of Polymer–Fullerene Blends. *Adv. Funct. Mater.* **20,** 3519–3529 (2010).

33. Rogers, J. T., Schmidt, K., Toney, M. F., Kramer, E. J. & Bazan, G. C. Structural Order in Bulk Heterojunction Films Prepared with Solvent Additives. *Adv. Mater.* **23,** 2284–2288 (2011).

34. Sharenko, A., Kuik, M., Toney, M. F. & Nguyen, T.-Q. Crystallization-Induced Phase Separation in Solution-Processed Small Molecule Bulk Heterojunction Organic Solar Cells. *Adv. Funct. Mater.* **24,** 3543–3550 (2014).

35. Moon, J. S. *et al.* Effect of Processing Additive on the Nanomorphology of a Bulk Heterojunction Material†. *Nano Lett.* **10,** 4005–4008 (2010).

36. Brady, M. A., Su, G. M. & Chabinyc, M. L. Recent progress in the morphology of bulk heterojunction photovoltaics. *Soft Matter* **7,** 11065 (2011).

37. Salleo, A., Kline, R. J., DeLongchamp, D. M. & Chabinyc, M. L. Microstructural Characterization and Charge Transport in Thin Films of Conjugated Polymers. *Adv. Mater.* **22,** 3812–3838 (2010).
38. DeLongchamp, D. M., Kline, R. J., Fischer, D. A., Richter, L. J. & Toney, M. F. Molecular Characterization of Organic Electronic Films. *Adv. Mater.* **23,** 319–337 (2011).
39. Rivnay, J., Mannsfeld, S. C. B., Miller, C. E., Salleo, A. & Toney, M. F. Quantitative Determination of Organic Semiconductor Microstructure from the Molecular to Device Scale. *Chem. Rev.* **112,** 5488–5519 (2012).
40. Müller-Buschbaum, P. The Active Layer Morphology of Organic Solar Cells Probed with Grazing Incidence Scattering Techniques. *Adv. Mater.* (2014). doi:10.1002/adma.201304187
41. Chabinyc, M. L. X-ray Scattering from Films of Semiconducting Polymers. *Polym. Rev.* **48,** 463–492 (2008).
42. Perez, L. A. *et al.* Effect of Backbone Regioregularity on the Structure and Orientation of a Donor–Acceptor Semiconducting Copolymer. *Macromolecules* **47,** 1403–1410 (2014).
43. Baker, J. L. *et al.* Quantification of Thin Film Crystallographic Orientation Using X-ray Diffraction with an Area Detector. *Langmuir* **26,** 9146–9151 (2010).
44. Rivnay, J., Noriega, R., Kline, R. J., Salleo, A. & Toney, M. F. Quantitative analysis of lattice disorder and crystallite size in organic semiconductor thin films. *Phys. Rev. B* **84,** 045203 (2011).

45. *Methods of X-Ray and Neutron Scattering in Polymer Science*. (Oxford University Press, Inc., 2000).

46. Rivnay, J. *et al.* Drastic Control of Texture in a High Performance n-Type Polymeric Semiconductor and Implications for Charge Transport. *Macromolecules* **44,** 5246–5255 (2011).

47. Tang, C., Wu, W., Smilgies, D.-M., Matyjaszewski, K. & Kowalewski, T. Robust Control of Microdomain Orientation in Thin Films of Block Copolymers by Zone Casting. *J. Am. Chem. Soc.* **133,** 11802–11809 (2011).

48. Babonneau, D. FitGISAXS: software package for modelling and analysis of GISAXS data using IGOR Pro. *J. Appl. Crystallogr.* **43,** 929–936 (2010).

49. Ilavsky, J. & Jemian, P. R. Irena: tool suite for modeling and analysis of small-angle scattering. *J. Appl. Crystallogr.* **42,** 347–353 (2009).

50. Müller-Buschbaum, P. Grazing incidence small-angle X-ray scattering: an advanced scattering technique for the investigation of nanostructured polymer films. *Anal. Bioanal. Chem.* **376,** 3–10 (2003).

51. Renaud, G., Lazzari, R. & Leroy, F. Probing surface and interface morphology with Grazing Incidence Small Angle X-Ray Scattering. *Surf. Sci. Rep.* **64,** 255–380 (2009).

Section I: Crystallization and Phase Seperation in Solution-Processed Small Molecule Bulk Heterojunction Organic Solar Cells Utilizing a Functionalized Fullerene Acceptor

A. *Section Introduction*

Given the strong dependence of BHJ OPV performance on blend phase separation, it is imperative to understand the thermodynamic driving forces and processes that lead to the formation of nanoscale phase separated, bicontinuous morphologies. Investigations of the much studied poly(3-hexylthiopene):phenyl-C_{61}-butyric acid methyl ester (P3HT:$PC_{61}BM$) OPV blend have found that in this system phase separation is largely the result of crystallization of the semicrystalline donor P3HT.[1–3] Solid state miscibility between the donor and acceptor has, however, also been demonstrated to directly affect BHJ morphology including the degree of donor-acceptor phase separation as well as the relative purity of mixed regions of amorphous donor and acceptor.[4–8] As polymer:fullerene BHJ blends dominate the literature[9], much less is known about the development of phase separation in OPVs that utilize solution-processed small molecule donor materials. Small molecule donors have, however, recently emerged as a viable alternative[10,11] to their polymer counterparts and offer several potential advantages in that they are monodisperse and can be purified with standard organic chemistry techniques. Knowledge of the driving forces for phase separation in solution-processed small molecule BHJ OPVs will therefore aid in the engineering of future high performing solar cells.

In this section the relationship between crystallization and phase separation in a solution-processed BHJ blend consisting of the small molecule donor 3,6-bis(5-(benzofuran-2-yl)thiophen-2-yl)-2,5-bis(2-ethylhexyl)pyrrolo[3,4-c]pyrrole-1,4-dione ($DPP(TBFu)_2$) and the fullerene electron acceptor $PC_{71}BM$ is investigated (Figure 5). This system was chosen because previous studies suggested that in optimized devices thermal annealing leads to increased phase separation and dramatic gains in power conversion efficiency (PCE).[12,13]

However, the driving forces for this behavior have not been previously investigated and it was therefore unclear what specific processes are responsible for this change in blend morphology and device performance. In-situ thermal annealing grazing incidence x-ray scattering is used to investigate the development of blend crystallinity and phase separation as a function of temperature and donor:acceptor blend ratio in order to better understand how thermal annealing leads to the formation of a BHJ morphology. Using these data we are able to correlate the formation of DPP(TBFu)$_2$ crystallites with the onset of phase separation in DPP(TBFu)$_2$:PC$_{71}$BM blends. Based on these x-ray scattering data as well as charge carrier mobility data extracted from *J-V* curves of single carrier diodes undergoing in-situ thermal annealing, it is hypothesized that, on the time scales and temperature ranges associated with the fabrication of optimized BHJ OPVs, blend phase separation is largely the result of donor crystallization. This observation is then used to explain the dramatic increase in performance induced by thermal annealing in higher performing donor:acceptor ratio DPP(TBFu)$_2$:PC$_{71}$BM BHJ OPVs as we directly correlate changes in blend morphology with solar cell figures of merit. A commercially available nucleating agent is then used during processing to modulate donor crystallization, and therefore the development of the bulk heterojunction morphology and device performance.

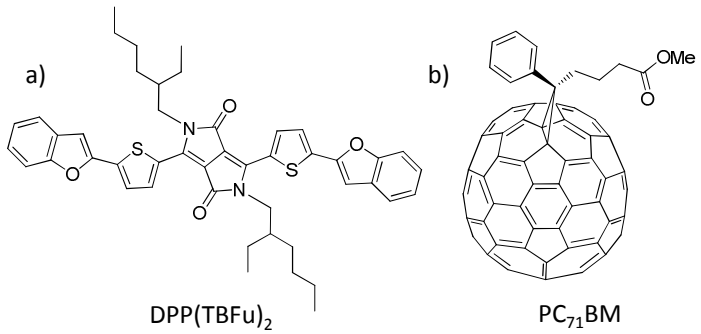

Figure 5: Chemical structures of the electron donor, DPP(TBFu)$_2$ (a), and electron acceptor, PC$_{71}$BM (b), used in this study.

B. Crystallization and Phase Separation as a Function of Annealing Temperature

In order to monitor blend morphological evolution as a function of temperature and therefore provide insight into the processes associated with the development of phase separation in solution-processed small molecule BHJ OPVs, both GIWAXS and GISAXS were performed on samples undergoing in-situ thermal annealing. This allowed donor or acceptor crystallization and donor-acceptor phase separation to be monitored during morphological development. DPP(TBFu)$_2$ crystallinity was quantified by fitting the DPP(TBFu)$_2$ (100) peak from GIWAXS spectra taken at various temperatures with a Pseudo-Voigt function. The Pseudo-Voigt peak area is a relative measure of the crystalline volume within the thin film. In neat films as well as in blends with PC$_{71}$BM, DPP(TBFu)$_2$ exhibits no signs of crystallinity in the as-cast state when spin-cast from chloroform. However, upon thermal annealing DPP(TBFu)$_2$ undergoes a cold crystallization similar to what has previously been observed in PC$_{61}$BM (Figure 6a).[14] We define the cold crystallization temperature (T_{CC}) as the temperature at which the DPP(TBFu)$_2$ (100) peak appears above the background scattering. In neat DPP(TBFu)$_2$ films the T_{CC} occurs at 50 ˚C. In DPP(TBFu)$_2$:PC$_{71}$BM blend films the DPP(TBFu)$_2$ T_{CC} increases with increasing PC$_{71}$BM content to 70 ˚C, 75 ˚C and 100 ˚C in 70:30, 50:50 and 30:70 DPP(TBFu)$_2$:PC$_{71}$BM blends by weight respectively (Figure 6b-d). The trend of increasing DPP(TBFu)$_2$ T_{CC} with increasing PC$_{71}$BM content can be explained in terms of DPP(TBFu)$_2$ dilution. As PC$_{71}$BM content increases, the concentration of DPP(TBFu)$_2$ nuclei likely decreases and thus the overall DPP(TBFu)$_2$ crystallization rate decreases, therefore increasing DPP(TBFu)$_2$'s T_{CC}. Similar T_{CC} trends have previously been observed in partially miscible polymer blends and explained as such.[15,16] The CCL of DPP(TBFu)$_2$ in both neat

and blend films follows a very similar trend to the relative peak area. This indicates that most of the increase in peak area after the T_{CC} can be attributed to the growth of existing DPP(TBFu)$_2$ crystallites as opposed to the nucleation of new crystallites. In the neat DPP(TBFu)$_2$ film and 70:30 blend samples the (100) peak area and CCL increase dramatically beginning at the T_{CC} and continuing over a narrow temperature range of approximately 10 degrees. They then only slightly increase as the temperature is further increased. The 50:50 blend sample's peak area and CCL exhibit the same dramatic increases beginning at the T_{CC} but then continue to gradually increase as temperature is further increased. The 30:70 blend exhibits somewhat different behavior from the other samples in that its peak area and CCL continually increase with an increase in temperature above T_{CC} without exhibiting the dramatic increases followed by a small or gradual increase characteristic of the other samples. Therefore as the fraction of $PC_{71}BM$ in the film increases, the nucleation of DPP(TBFu)$_2$ crystallites requires higher temperatures and becomes a more gradual process. Importantly, no $PC_{71}BM$ crystallization was observed in any of the DPP(TBFu)$_2$:$PC_{71}BM$ blend films in the temperature ranges investigated during this study.

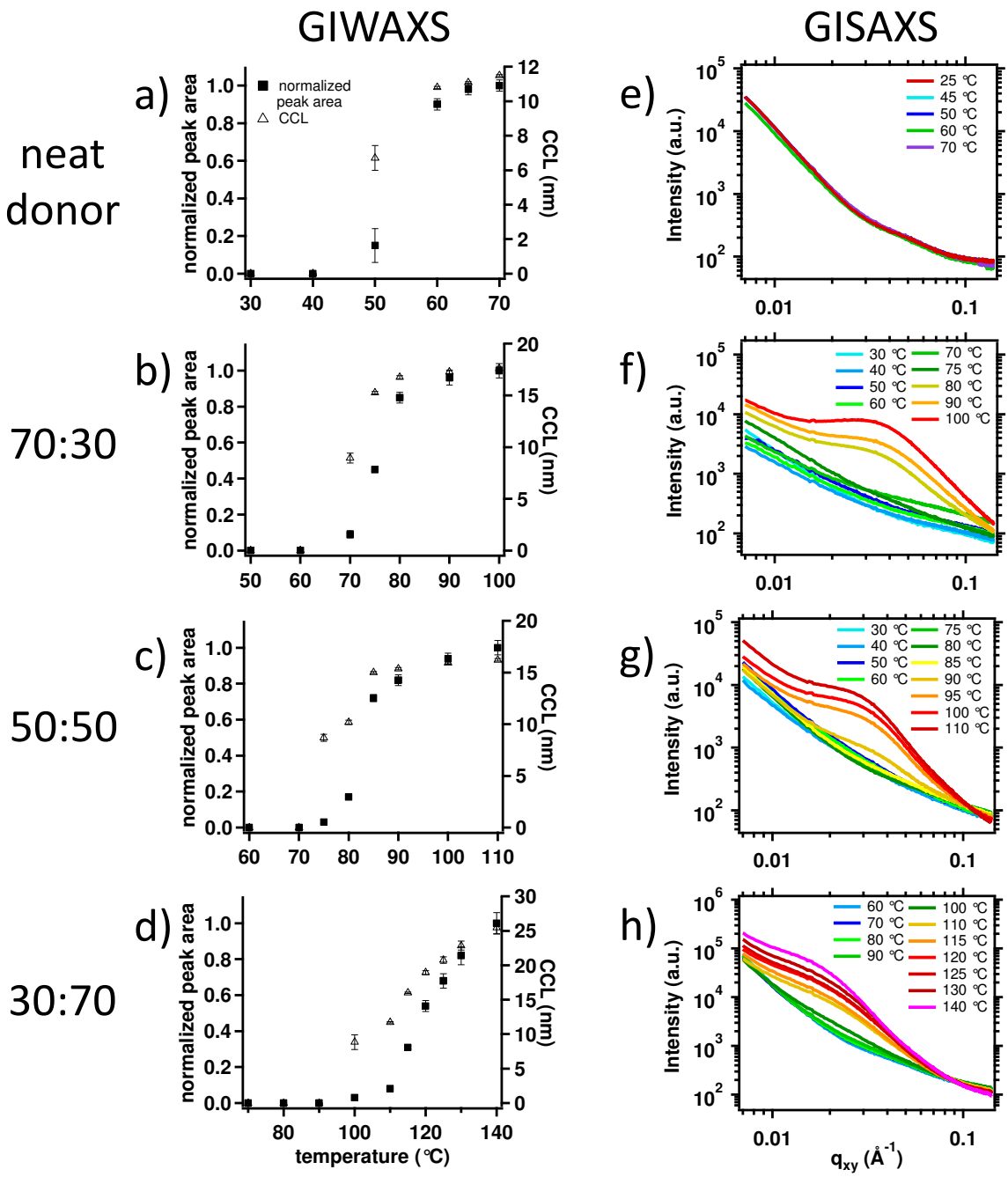

Figure 6: In-situ thermal annealing GIWAXS (a-d) and GISAXS (e-h) of a neat DPP(TBFu)$_2$ film (a, e) as well as DPP(TBFu)$_2$:PC$_{71}$BM blend films (b-d, f-h). Reprinted with permission. © 2014 WILEY-VCH Verlag GmbH & Co. KGaA, Weinheim.

To facilitate a direct comparison of thin film crystallinity and phase separation, in-situ thermal annealing GISAXS measurements were performed on samples fabricated identically to those used for in-situ GIWAXS and measured over the same temperature range (Figure

6e-h). Figure 6e shows in-situ thermal annealing GISAXS data for a neat film of DPP(TBFu)$_2$ from 25 to 70 ˚C. The in-plane line scans show no significant change even though in-situ thermal annealing GIWAXS measurements have shown that DPP(TBFu)$_2$ undergoes a cold crystallization in this temperature range. We therefore conclude that the electron density differences between amorphous and crystalline regions of DPP(TBFu)$_2$ are not significant enough to produce a peak in scattered intensity. We can then reason that any peaks in the scattered intensity exhibited by DPP(TBFu)$_2$:PC$_{71}$BM blend films are the result of electron density differences between DPP(TBFu)$_2$-rich and PC$_{71}$BM-rich phases. Figures 3f-h display in-situ thermal annealing GISAXS data of 70:30, 50:50 and 30:70 DPP(TBFu)$_2$:PC$_{71}$BM blend films. Each blend ratio exhibits similar behavior. As-cast blends display only the same monotonically decreasing intensity seen in films of neat DPP(TBFu)$_2$. Thus, the as-cast blends lack sufficient electron density to produce a peak in scattered intensity indicating that these samples consist of an intimately mixed donor-acceptor morphology. As the blends are heated, however, a peak develops at some transition temperature indicating the appearance of differences in electron density in the film which is interpreted as the onset of donor-acceptor phase separation. The GISAXS peak shifts slightly to smaller q values with increasing PC$_{71}$BM content indicating phase separation is occurring on a larger length scale with increasing PC$_{71}$BM content. Most interestingly, in each blend the temperature at which this transition from homogeneously mixed to phase separated morphology occurs closely correlates with the nucleation of DPP(TBFu)$_2$ crystallites as measured using the in-situ thermal annealing GIWAXS discussed above. The development of phase separation in each of the different blend ratios also follows the same trend exhibited by the in-situ GIWAXS measurements. Specifically, the 70:30 blend transitions from a homogeneous blend to a phase separated morphology over a relatively narrow temperature

range and the 50:50 blend transitions slightly more gradually whereas the 30:70 blend gradually and continuously phase separates with increasing temperature. In both the 70:30 and 50:50 blends, phase separation occurs at the temperature immediately following the dramatic increase in peak area exhibited by in-situ GIWAXS. The 30:70 blend, however, begins to phase separate at the temperature that corresponds to the onset of DPP(TBFu)$_2$ crystallization, i.e. DPP(TBFu)$_2$'s T_{CC}.

C. Effect of Crystallization and Phase Separation on Device Optical and Electrical Properties

Photoluminescence (PL) measurements of as-cast blend films as well as blend films that had been annealed above their respective DPP(TBFu)$_2$ T_{CC} were used to further verify our interpretation of the presented GISAXS data (Figure 7). For each blend, annealed films exhibit PL spectra identical to that of neat DPP(TBFu)$_2$. The PL spectra of as-cast blends, however, are shifted to lower energy and broadened compared to those of the annealed blends and neat DPP(TBFu)$_2$. This lower energy, broader PL spectra likely originates from the DPP(TBFu)$_2$:$PC_{71}BM$ charge transfer (CT) state.[17,18] In order for the CT state emission to dominate emission from DPP(TBFu)$_2$, the blend must consist of a well-mixed morphology that maximizes DPP(TBFu)$_2$:$PC_{71}BM$ interfacial surface area while lacking neat DPP(TBFu)$_2$ domains larger than the exciton diffusion length.[19,20] Conversely, for neat DPP(TBFu)$_2$ emission to dominate CT state emission, the blend morphology must consist of a significant amount of neat DPP(TBFu)$_2$ domains larger than the exciton diffusion length. PL and GISAXS measurements then both indicate that as-cast blends consist of an intimately mixed morphology, but that when blend films are annealed above DPP(TBFu)$_2$'s T_{CC} they phase separate. These measurements of bulk morphological properties are also consistent

with previous atomic force microscopy measurements of surface topography which indicated phase separation upon thermal annealing.[12] However, we have now importantly correlated the development of bulk phase separation with the onset of DPP(TBFu)$_2$ crystallization. We thus hypothesize that the development of DPP(TBFu)$_2$:PC$_{71}$BM blend phase separation is the direct result of DPP(TBFu)$_2$ crystallization from an initially homogeneously mixed, amorphous donor:acceptor film. We propose that as DPP(TBFu)$_2$ nuclei form and grow they expel PC$_{71}$BM molecules, simultaneously creating DPP(TBFu)$_2$-rich domains, consisting largely of DPP(TBFu)$_2$ crystallites, and PC$_{71}$BM-rich domains, formed from previously mixed regions of the film that have been enriched with PC$_{71}$BM during DPP(TBFu)$_2$ crystallization.

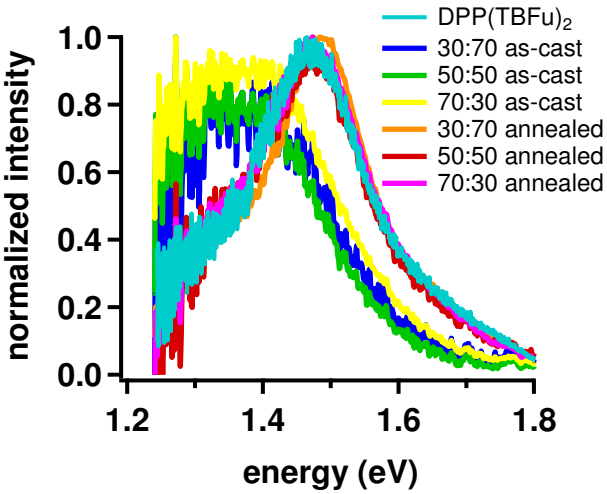

Figure 7: Photoluminescence spectra of a neat DPP(TBFu)$_2$ film as well as as-cast and annealed DPP(TBFu)$_2$:PC$_{71}$BM blend films. The annealed 70:30, 50:50 and 30:70 blend films were annealed at 100, 110 and 150 ˚C respectively for 2 minutes each in a nitrogen environment. Reprinted with permission. © 2014 WILEY-VCH Verlag GmbH & Co. KGaA, Weinheim.

If phase separation is the result of DPP(TBFu)$_2$ crystallization, the nucleation and growth of DPP(TBFu)$_2$ crystallites should correlate with an increase in blend electron mobility as increased phase separation leads to aggregation and percolation of PC$_{71}$BM, the electron

transporting phase. To confirm this behavior, electron-only diodes of a 70:30 DPP(TBFu)$_2$:PC$_{71}$BM blend were fabricated. Diode *J-V* curves were then measured during in-situ thermal annealing over the same temperature range investigated with in-situ thermal annealing GIWAXS and GISAXS and mobility values extracted by fitting these data to the Mott-Gurney relation for space charge-limited current (Figure 5). In the as-cast 70:30 blend film the electron mobility is 2.0 x 10^{-6} cm^2/Vs, 3 orders of magnitude lower than the diode electron mobility of a neat PCBM film, likely due to a lack of percolated PC$_{71}$BM networks in the homogeneous as-cast morphology.[21] The electron mobility remains low with increasing thermal annealing temperature until dramatically increasing approximately 2 orders of magnitude at 90 ˚C to 3.3 x 10^{-4} cm^2/Vs. In organic semiconductors, charge carriers move by a thermally activated hopping process between localized states. Thus, some increase in mobility is expected with increasing sample temperature. Based on PCBM's hopping activation energy we would expect the electron mobility to approximately double with an increase in temperature from 80 to 100 ˚C.[22] The observed increase in electron mobility is thus far greater than can be explained by increased thermal hopping activation alone. Based on this observation as well as the fact that the mobility increases from a value orders of magnitude lower than that of neat PCBM to approaching that of neat PCBM, we explain this dramatic increase in electron mobility as a consequence of the development of percolated networks of PC$_{71}$BM that form as a result of DPP(TBFu)$_2$ crystallization and concurrent PC$_{71}$BM aggregation. This interpretation of the data is further supported given the close correlation of the dramatic increase in the relative crystallinity of DPP(TBFu)$_2$ as measured by in-situ thermal annealing GIWAXS, the temperature at which phase separation develops as determined by in-situ thermal annealing GISAXS and the temperature at which the electron mobility significantly increased. The slightly higher temperature at which the

increase in electron mobility is observed as compared to the development of phase separation measured with GISAXS could be because further phase separation needs to occur before the aggregated $PC_{71}BM$ domains form a percolated network necessary for high electron mobility in the blend. Therefore not only does $DPP(TBFu)_2$ crystallization lead to blend phase separation but that in 70:30 blends this phase separation then leads to a dramatic increase in electron mobility, presumably due to the formation of a percolated network of aggregated $PC_{71}BM$ domains.

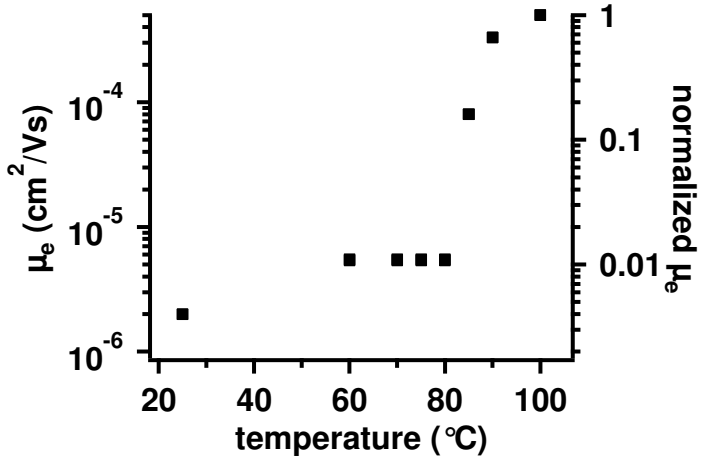

Figure 8: Electron mobility (μ_e) of a 70:30 $DPP(TBFu)_2$:$PC_{71}BM$ diode measured during in-situ thermal annealing. Data collected by Dr. Martijn Kuik using a temperature controlled probe station evacuated to ~10^{-7} Torr. Reprinted with permission. © 2014 WILEY-VCH Verlag GmbH & Co. KGaA, Weinheim.

Previous work demonstrated that BHJ OPV performance in the as-cast 70:30 blend is very low but that upon thermal annealing both short-circuit current density (J_{sc}) and fill factor (FF) (and therefore PCE) dramatically increase.[12] A 70:30 $DPP(TBFu)_2$:$PC_{71}BM$ BHJ OPV device was therefore serially annealed over a temperature range similar to what has been investigated with in-situ thermal annealing GIWAXS, GISAXS and electron only diode measurements so that the increase in solar cell figures of merit could be compared with the changes in film morphology and charge transport discussed above. Figure 9 displays the J_{sc}

and FF of a 70:30 OPV device that was serially annealed at the given temperature values. The J_{sc} and FF are initially very low, 0.43 mA/cm^2 and 0.23, respectively, but dramatically increase to 5.35 mA/cm^2 and 0.36 when annealed at 90 ˚C. This is the same temperature the blend electron mobility was observed to dramatically increase via in-situ thermal annealing of electron only diodes of 70:30 DPP(TBFu)$_2$:PC$_{71}$BM blends. The strong correlation between the dramatic increases in electron mobility and J_{sc} and FF is consistent with previous investigations that have shown that, in general, recombination decreases, and thus J_{sc} and FF increase, as charge carrier mobility increases.[23,24] While we are now comparing an ex-situ measurement (serial annealing) to an in-situ measurement (blend electron mobility), the strong correlation between data from the two types of measurements suggests this is a valid comparison. Some of this increase in J_{sc} and FF, however, is probably additionally attributed to the approximately order of magnitude increase in hole mobility that also occurs over this temperature range, likely due to the increase in the solid state order of DPP(TBFu)$_2$, the hole transporting phase (Table 1). The lower OPV performance exhibited here compared to previous reports[12] can be attributed to the shorter, serialized annealing in this study as opposed to the optimized, longer, single annealing step previously used to achieve higher efficiency. From the presented data, it is clear that crystallization, the development of blend phase separation and a significant increase in blend electron mobility and OPV figures of merit all dramatically increase over the same narrow temperature range during thermal annealing.

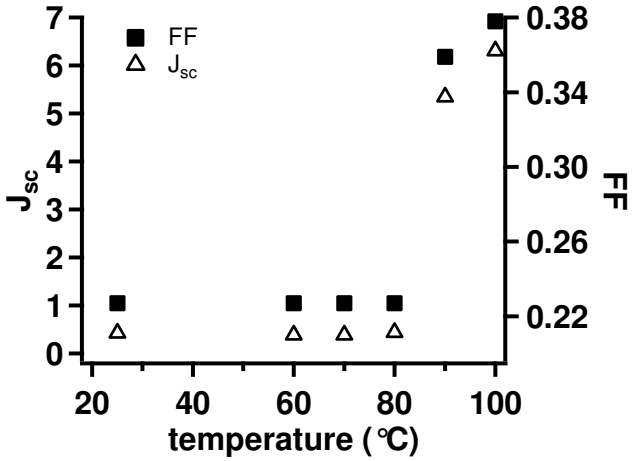

Figure 9: J_{sc} and FF of a 70:30 DPP(TBFu)$_2$:PC$_{71}$BM BHJ OPV device series annealed at the indicated temperatures. Reprinted with permission. © 2014 WILEY-VCH Verlag GmbH & Co. KGaA, Weinheim.

Table 1: Hole mobility of as-cast and annealed 70:30 DPP(TBFu)$_2$:PC$_{71}$BM blend films.

processing condition	hole mobility (cm^2/Vs)
as-cast	2.0 X 10^{-5}
annealed 2 min, 100 ˚C	1.1 X 10^{-4}

D. Long Time, Low Temperature Thermal Annealing of BHJ Blends

In order to investigate the influence DPP(TBFu)$_2$:PC$_{71}$BM solid state immiscibility has on phase separation 70:30, 50:50 and 30:70 blend films were annealed for 48 hours at 60 ˚C. If solid state immiscibility between the two materials is acting as a significant driving force for phase separation, perhaps via a spinodal decomposition process, it was hypothesized that samples held at an elevated temperature that facilitated solid state diffusion, but below DPP(TBFu)$_2$'s T_{CC}, and allowed time to approach equilibrium, would exhibit blend phase separation without DPP(TBFu)$_2$ crystallization. This experiment was therefore an attempt to decouple DPP(TBFu)$_2$ crystallization and blend phase separation. Figure 10 shows the GISAXS line scans and GIWAXS 1D integrations of these samples. By comparing as-cast and annealed line cuts in Figure 10a we can deduce that the 70:30 blend ratio sample

developed some amount of phase separation based on the small peak it displays that is not present in the as-cast sample. Likewise, the 50:50 blend exhibits an even smaller degree of phase separation based on the slight increase in intensity of the annealed film at high q values compared to the as-cast film. However, the 30:70 blend display a negligible amount of phase separation during the 48 hour, 60 ˚C anneal based on the very similar shape of the as-cast and annealed line cuts. Interestingly, Figure 10b shows that the 70:30 film displays some amount of $DPP(TBFu)_2$ crystallization based on the strength of the $DPP(TBFu)_2$ (100) peak and the 50:50 blend exhibits a small amount of $DPP(TBFu)_2$ crystallization based on the very weak (100) peak intensity. The 30:70 blend, however, displays no signs of $DPP(TBFu)_2$ crystallization as the peaks at 0.68, 1.31 and 1.90 $Å^{-1}$ associated with $PC_{71}BM$ dominate the spectra and the $DPP(TBFu)_2$ (100) peak is absent. As phase separation once again correlates with $DPP(TBFu)_2$ crystallization and is absent in blends that lack $DPP(TBFu)_2$ crystallization, it is hypothesized that while $DPP(TBFu)_2$ and $PC_{71}BM$ may be less than perfectly miscible, $DPP(TBFu)_2$ crystallization is the primary driving force for the development of blend phase separation. This is not to say that miscibility plays no role in the development of blend phase separation, however, as the degree to which $PC_{71}BM$ is soluble in the amorphous $DPP(TBFu)_2$:$PC_{71}BM$ matrix will affect how easily $PC_{71}BM$-rich domains form,[25,26] and thus how easily $PC_{71}BM$ percolation is achieved as $PC_{71}BM$ is aggregated during $DPP(TBFu)_2$ crystallization. Nonetheless, as the data indicate that the development of a nanoscale phase separated, bicontinuous morphology is initiated by the formation of $DPP(TBFu)_2$ crystallites, we assign $DPP(TBFu)_2$ crystallization as the primary driving force and thus the essential process responsible for the development of blend phase separation in the samples studied here. We also note that these results imply that $DPP(TBFu)_2$'s T_{CC} has some kinetic dependence, i.e. the T_{CC} can be shifted to lower temperatures given sufficiently

long annealing times, which follows from well-established crystallization theory.[27] As all in-situ thermal annealing experiments were performed on extremely similar time scales, this kinetic dependence does not affect our interpretation of the presented data.

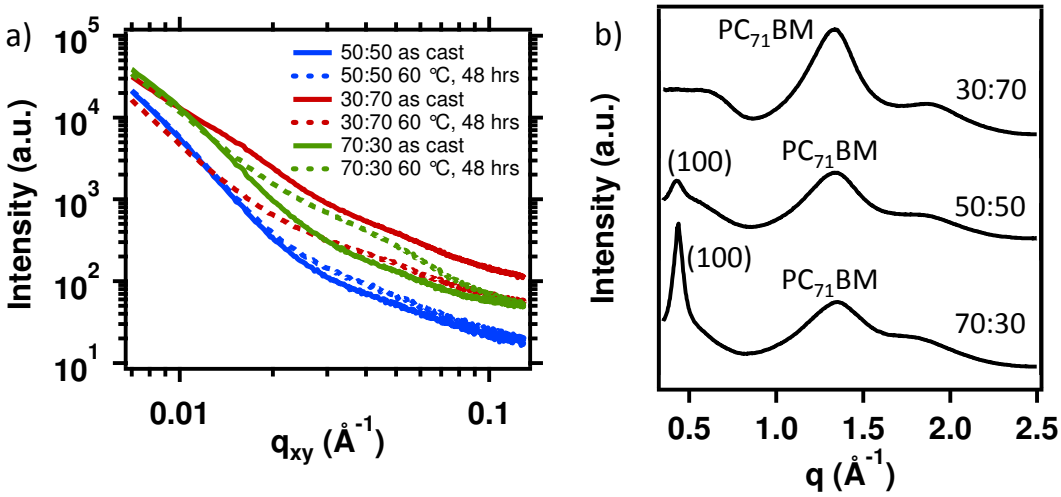

Figure 10: a) GISAXS in-plane line scans of as-cast DPP(TBFu)$_2$:$PC_{71}BM$ blend films as well as blend films annealed at 60 ˚C for 48 hours. b) 1D GIWAXS radial integrations of DPP(TBFu)$_2$:$PC_{71}BM$ blend films annealed at 60 ˚C for 48 hours. Reprinted with permission. © 2014 WILEY-VCH Verlag GmbH & Co. KGaA, Weinheim.

E. The Effect of a Commercially Available Nucleating Agent on Device Processing

The work presented thus far demonstrates that crystallization of the donor molecule is extremely important in BHJ OPV devices fabricated using small molecule donors and the fullerene acceptor phenyl-C_{71}-butyric acid methyl ester ($PC_{71}BM$). Likewise, control of polymer crystallization has proven essential for the manufacture of many consumer products. Nucleating agents are widely used to control crystallization in commodity polymers in order to tailor their mechanical, thermal and optical properties.[28–30] More recently, nucleating agents functionality has been extended to organic electronics as they have been used to increase the device yield and processability of solution-processed organic field-effect transistors as well as limit the size of PCBM crystallites upon thermal annealing.[31,32] It was

therefore hypothesized that commercially available nuvleating agents could be used to control the crystallization, and therefore BHJ development, in solution-processed small molecule BHJ OPVs. A sample of 1,3:2,4-bis(3,4-dimethylbenzylidene)sorbitol (DMDBS; Millad 3988), a nucleating agent commonly used to clarify isotactic polypropylene, was obtained from Milliken Chemical (Figure 11). Figure 12 displays J_{sc} as a function of isothermal annealing time for DPP(TBFu)$_2$:PC$_{71}$BM BHJ OPV devices processed without and with 1.4 wt. % DMDBS. Both devices display near identical J_{sc} in the as-cast state, approximately 0.45 mA/cm^2. However, the devices cast without and with nucleating agent respond drastically different to the isothermal annealing with the J_{sc} of the device processed with DMDBS increasing significantly faster than the device processed without DMDBS. The J_{sc} of the device processed with DMDBS increases to 4.62 mA/cm^2 after 22 minutes whereas the device processed without DMDBS does not exhibit a comparable J_{sc} until approximately 44 minutes of annealing.

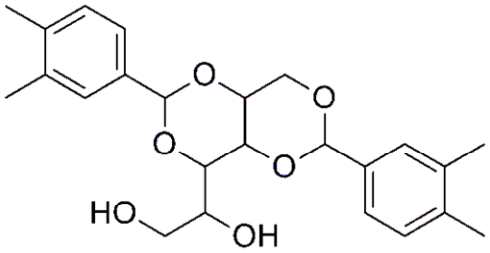

DMDBS

Figure 11: Chemical structure of the nucleating agent 1,3:2,4-bis(3,4-dimethylbenzylidene)sorbitol (DMDBS; Millad 3988).

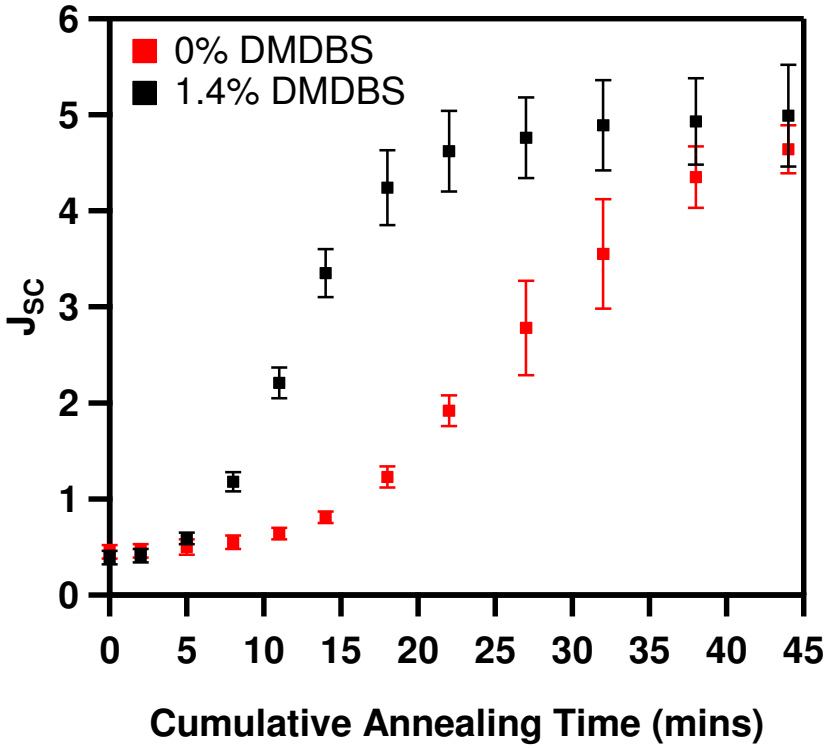

Figure 12: J_{sc} as a function of isothermal annealing time at 80 ˚C for 70:30 DPP(TBFu)$_2$:PC$_{71}$BM BHJ OPV devices. Error bars denote the first standard deviation calculated from 12 different devices of each condition fabricated over multiple days. Reproduced from Sharenko, A. *et al.* Use of a commercially available nucleating agent to control the morphological development of solution-processed small molecule bulk heterojunction organic solar cells. *J. Mater. Chem. A* (2014). doi:10.1039/C4TA03469D with permission from The Royal Society of Chemistry.

As explained below, it is inferred that the accelerated increase in J_{sc} as a function of isothermal annealing exhibited by the device processed with DMDBS compared to the device processed without DMDBS is the result of a faster DPP(TBFu)$_2$ nucleation rate leading to faster crystallization kinetics in the presence of DMDBS. This interpretation of the data is consistent with the observation that, in DPP(TBFu)$_2$:PC$_{71}$BM BHJ OPV devices, DPP(TBFu)$_2$ crystallization leads to increased phase separation and a concomitant increase in J_{sc}, thus directly linking donor crystallization to increased J_{sc}.[33] Additionally, this interpretation is consistent with the fact that sorbitol-based nucleating agents were developed to accelerate the primary nucleation rate of iPP during solidification from the melt[34–36] and

have more recently demonstrated the ability to modulate the crystallization of a variety of organic semiconductors.[31] According to classic nucleation theory, nucleating agents improve the rate of primary nucleation by reducing the driving force needed to form a stable nuclei, resulting in an increase in the overall crystallization rate of a material.[37] It therefore appears that DMDBS is remarkably able to have a similar effect on the molecular semiconductor DPP(TBFu)$_2$ in a DPP(TBFu)$_2$:PC$_{71}$BM BHJ OPV blend.

Further evidence for this hypothesis was collected using in-situ isothermal annealing GIWAXS experiments, which were performed on DPP(TBFu)$_2$:PC$_{71}$BM BHJ blend films cast without and with DMDBS**.** The data in Figure 13 reveal that the crystallization kinetics of DPP(TBFu)$_2$ are faster with DMDBS compared to without. To quantify this difference the in-situ isothermal annealing GIWAXS data was fit using Avrami kinetics[38–40] as described by Equation 5:

$$F = 1 - \exp[-(kt)^n] \quad (5)$$

Where F is the fractional crystallization at time t, k is a temperature dependent rate constant and n is referred to as the Avrami exponent, which is often interpreted as indicative of the geometry or dimensionality of the crystallization process. The results of this fitting process are displayed in Table 2. DPP(TBFu)$_2$:PC$_{71}$BM BHJ blend films without and with DMDBS exhibit essentially the same Avrami constant, suggesting DMDBS does not significantly alter the crystallization geometry or dimensionality. The overall crystallization rate constant for the two samples, however, differs with the film prepared with DMDBS having a rate constant approximately 1.5 times greater than the film prepared without DMDBS. This increased rate constant for DPP(TBFu)$_2$:PC$_{71}$BM BHJ blends prepared with DMDBS is consistent with the data in Figure 12 and confirms that incorporation of DMDBS into

DPP(TBFu)$_2$:PC$_{71}$BM BHJ blend films leads to accelerated DPP(TBFu)$_2$ crystallization kinetics.

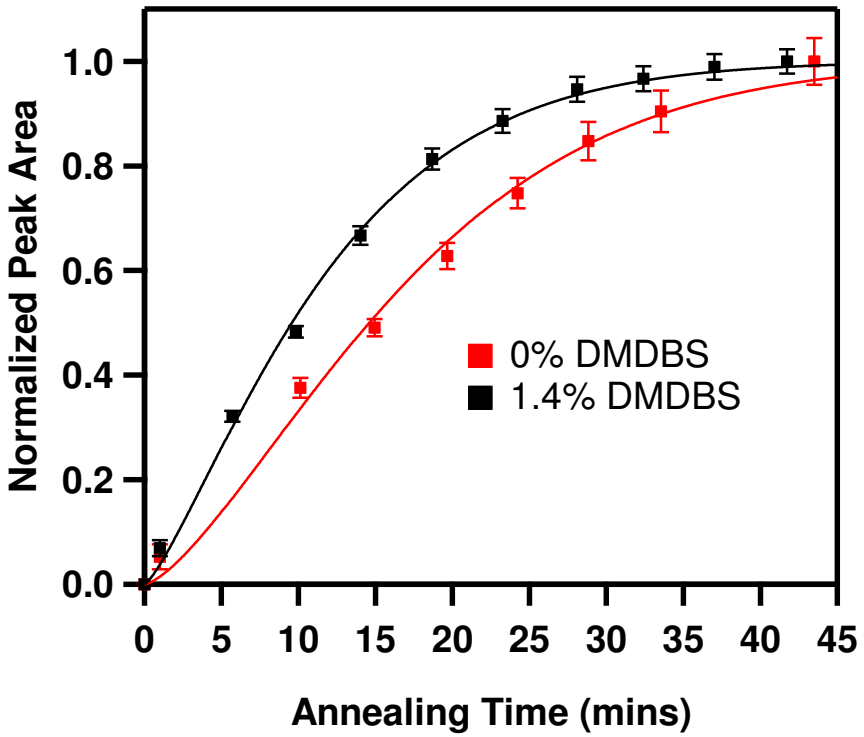

Figure 13: In-situ isothermal annealing GIWAXS at 80 ˚C for 70:30 DPP(TBFu)$_2$:PC$_{71}$BM BHJ films with and without DMDBS. The y-axis is the normalized peak area of the DPP(TBFu)$_2$ (100) reflection integrated over all polar angles. The normalization was done to longest times. Solid lines are Avrami fits to the data. Reproduced from Sharenko, A. *et al.* Use of a commercially available nucleating agent to control the morphological development of solution-processed small molecule bulk heterojunction organic solar cells. *J. Mater. Chem. A* (2014). doi:10.1039/C4TA03469D with permission from The Royal Society of Chemistry.

Table 2: Avrami parameters extracted from fits to the in-situ isothermal GIWAXS data in Figure 13. R^2 is the coefficient of determination for the fits. Wt. % expressed as a percentage of total donor and acceptor weight in solution.

DMDBS [wt. %]	**n**	**k**	**R^2**
0	1.44 ± 0.10	0.053 ± 0.001	0.9931
1.4	1.28 ± 0.05	0.078 ± 0.001	0.9978

DMDBS does not appear to change the crystal structure or crystalline texture of DPP(TBFu)$_2$:PC$_{71}$BM BHJ blends as evidenced by Figure 14. This would be consistent with the similar Avrami exponents for the blend without and with the nucleating agent as determined from the data in Figure 13.

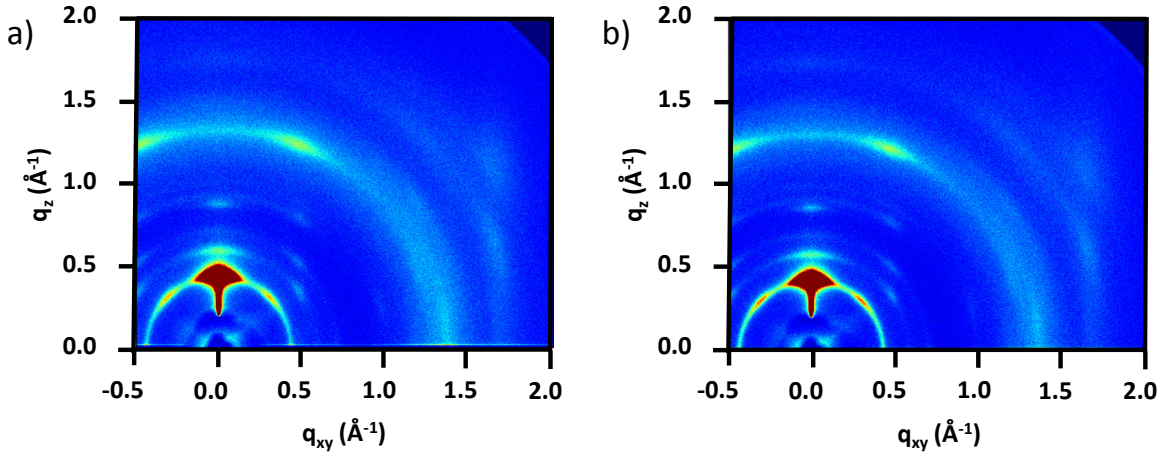

Figure 14: 2D GIWAXS images of 70:30 DPP(TBFu)$_2$:PC$_{71}$BM BHJ films without (a) and with (b) 1.4 wt. % DMDBS after isothermal anneal at 80 ˚C for 47 mins. Normalized peak area data in Figure 10 was calculated using the DPP(TBFu)$_2$ (100) peak at q_z = 0.43 Å^{-1}. Reproduced from Sharenko, A. *et al.* Use of a commercially available nucleating agent to control the morphological development of solution-processed small molecule bulk heterojunction organic solar cells. *J. Mater. Chem. A* (2014). doi:10.1039/C4TA03469D with permission from The Royal Society of Chemistry.

F. Section Conclusion

Using in-situ thermal annealing GIWAXS, GISAXS and electron only diode measurements as well as PL spectra of as-cast and annealed films it has been demonstrated that in DPP(TBFu)$_2$:PC$_{71}$BM blends donor crystallization is the driving force for the development of the nanoscale phase separated, bicontinuous morphology necessary for the fabrication of efficient BHJ OPVs. Specifically, it has been shown that thermal annealing causes donor crystallization in neat donor films as well as donor:acceptor blend films and that in blend films this crystallization leads to the formation of donor-rich and acceptor-rich

domains. In higher performing donor:acceptor ratio devices the formation of these acceptor-rich domains leads to dramatic increases in blend electron mobility and device J_{sc} and FF (and thus overall device performance). Our results therefore suggest that small molecule donor crystallization is important for reasons other than the increase in charge carrier mobility associated with order in molecular species. We have shown that phase separation in the DPP(TBFu)$_2$:PC$_{71}$BM system is induced via donor crystallization much like what has been observed in the P3HT:PCBM BHJ OPV system. However, P3HT is semicrystalline and therefore generally not considered representative of the largely structurally disordered donor polymers utilized by high performing polymer:PCBM BHJ OPVs.[7,8,25,41] In contrast, it is proposed that because many small molecule donors have shown evidence of crystallization, the trends we have observed in the DPP(TBFu)$_2$:PC$_{71}$BM system are likely more generally applicable to other small molecule donor:PCBM systems. This is additionally evidenced by the correlation between crystallization and phase separation exhibited by other efficient small molecule donor:PCBM BHJ OPVs.[42] Accordingly, the commercially available nucleating agent DMDBS was used to successfully control small molecule donor crystallization, and therefore BHJ morphological development, in the DPP(TBFu)$_2$:PC$_{71}$BM BHJ OPV system. It was shown that DMDBS is capable of accelerating donor molecule crystallization kinetics. The ability to accelerate donor molecule crystallization kinetics has important implications for BHJ OPV device fabrication, where the use of nucleating agents could potentially lead to shorter thermal annealing protocols, thus leading to more economical device manufacturing, or help overcome kinetic barriers to crystallization that prevent the formation of optimized BHJ morphologies.[43] This section has therefore developed useful processing-property-performance relationships for solution-processed small molecule organic solar cells utilzing PCBM as an electron acceptor. Such knowledge

will likely be essential as this promising photovoltaic technology attempts to transition from an academic curiosity to a commercially viable renewable energy technology.

G. References

1. Treat, N. D. *et al.* Interdiffusion of PCBM and P3HT Reveals Miscibility in a Photovoltaically Active Blend. *Adv. Energy Mater.* **1,** 82–89 (2011).
2. Chen, D., Liu, F., Wang, C., Nakahara, A. & Russell, T. P. Bulk Heterojunction Photovoltaic Active Layers via Bilayer Interdiffusion. *Nano Lett.* **11,** 2071–2078 (2011).
3. Kozub, D. R. *et al.* Polymer Crystallization of Partially Miscible Polythiophene/Fullerene Mixtures Controls Morphology. *Macromolecules* **44,** 5722–5726 (2011).
4. Treat, N. D. *et al.* Polymer-Fullerene Miscibility: A Metric for Screening New Materials for High-Performance Organic Solar Cells. *J. Am. Chem. Soc.* **134,** 15869–15879 (2012).
5. Ma, W., Ye, L., Zhang, S., Hou, J. & Ade, H. Competition between morphological attributes in the thermal annealing and additive processing of polymer solar cells. *J. Mater. Chem. C* **1,** 5023–5030 (2013).
6. Ma, W. *et al.* Domain Purity, Miscibility, and Molecular Orientation at Donor/Acceptor Interfaces in High Performance Organic Solar Cells: Paths to Further Improvement. *Adv. Energy Mater.* **3,** 864–872 (2013).
7. Collins, B. A. *et al.* Absolute Measurement of Domain Composition and Nanoscale Size Distribution Explains Performance in PTB7:PC71BM Solar Cells. *Adv. Energy Mater.* **3,** 65–74 (2013).

8. Tumbleston, J. R., Stuart, A. C., Gann, E., You, W. & Ade, H. Fluorinated Polymer Yields High Organic Solar Cell Performance for a Wide Range of Morphologies. *Adv. Funct. Mater.* **23,** 3463–3470 (2013).
9. Thompson, B. C. & Fréchet, J. M. J. Polymer–Fullerene Composite Solar Cells. *Angew. Chem. Int. Ed.* **47,** 58–77 (2008).
10. Van der Poll, T. S., Love, J. A., Nguyen, T.-Q. & Bazan, G. C. Non-Basic High-Performance Molecules for Solution-Processed Organic Solar Cells. *Adv. Mater.* **24,** 3646–3649 (2012).
11. Zhou, J. *et al.* Solution-Processed and High-Performance Organic Solar Cells Using Small Molecules with a Benzodithiophene Unit. *J. Am. Chem. Soc.* **135,** 8484–8487 (2013).
12. Walker, B. *et al.* Nanoscale Phase Separation and High Photovoltaic Efficiency in Solution-Processed, Small-Molecule Bulk Heterojunction Solar Cells. *Adv. Funct. Mater.* **19,** 3063–3069 (2009).
13. Dang, X.-D. *et al.* Nanostructure and Optoelectronic Characterization of Small Molecule Bulk Heterojunction Solar Cells by Photoconductive Atomic Force Microscopy. *Adv. Funct. Mater.* **20,** 3314–3321 (2010).
14. Verploegen, E. *et al.* Effects of Thermal Annealing Upon the Morphology of Polymer–Fullerene Blends. *Adv. Funct. Mater.* **20,** 3519–3529 (2010).
15. Siciliano, A. *et al.* Miscibility and Thermal and Crystallization Behaviors of Poly(D-(-)-3-hydroxybutyrate)/Atactic Poly(methyl methacrylate) Blends. *Macromolecules* **28,** 8065–8072 (1995).
16. Zhang, L., Goh, S. H. & Lee, S. Y. Miscibility and crystallization behaviour of poly(l-lactide)/poly(p-vinylphenol) blends. *Polymer* **39,** 4841–4847 (1998).

17. Zhou, Y. *et al.* Observation of a Charge Transfer State in Low-Bandgap Polymer/Fullerene Blend Systems by Photoluminescence and Electroluminescence Studies. *Adv. Funct. Mater.* **19,** 3293–3299 (2009).
18. Tvingstedt, K. *et al.* Electroluminescence from Charge Transfer States in Polymer Solar Cells. *J. Am. Chem. Soc.* **131,** 11819–11824 (2009).
19. Tvingstedt, K., Vandewal, K., Zhang, F. & Inganäs, O. On the Dissociation Efficiency of Charge Transfer Excitons and Frenkel Excitons in Organic Solar Cells: A Luminescence Quenching Study. *J. Phys. Chem. C* **114,** 21824–21832 (2010).
20. Riisness, I. & Gordon, M. J. Electronic structure disorder, vibronic coupling, and charge transfer excitons in poly(fluorene-alt-bithiophene):fullerene films. *Appl. Phys. Lett.* **102,** 113302 (2013).
21. Mihailetchi, V. d. *et al.* Electron Transport in a Methanofullerene. *Adv. Funct. Mater.* **13,** 43–46 (2003).
22. Craciun, N. I., Wildeman, J. & Blom, P. W. M. Universal Arrhenius Temperature Activated Charge Transport in Diodes from Disordered Organic Semiconductors. *Phys. Rev. Lett.* **100,** 056601 (2008).
23. Proctor, C. M., Kim, C., Neher, D. & Nguyen, T.-Q. Nongeminate Recombination and Charge Transport Limitations in Diketopyrrolopyrrole-Based Solution-Processed Small Molecule Solar Cells. *Adv. Funct. Mater.* **23,** 3584–3594 (2013).
24. Wagenpfahl, A., Deibel, C. & Dyakonov, V. Organic Solar Cell Efficiencies Under the Aspect of Reduced Surface Recombination Velocities. *IEEE J. Sel. Top. Quantum Electron.* **16,** 1759–1763 (2010).

25. Bartelt, J. A. *et al.* The Importance of Fullerene Percolation in the Mixed Regions of Polymer–Fullerene Bulk Heterojunction Solar Cells. *Adv. Energy Mater.* **3,** 364–374 (2012).
26. Vakhshouri, K., Kozub, D. R., Wang, C., Salleo, A. & Gomez, E. D. Effect of Miscibility and Percolation on Electron Transport in Amorphous Poly(3-Hexylthiophene)/Phenyl-C_{61}-Butyric Acid Methyl Ester Blends. *Phys. Rev. Lett.* **108,** 026601 (2012).
27. Mandelkern, L. *Crystallization of Polymers*. **2: Kinetics and Mechanisms,** (Cambridge University Press, 2004).
28. Dufton, P. *Functional Additives for the Plastics Industry: Trends in Use*. (Rapra Technology Limited, 1998).
29. Kristiansen, M., Tervoort, T., Smith, P. & Goossens, H. Mechanical Properties of Sorbitol-Clarified Isotactic Polypropylene: Influence of Additive Concentration on Polymer Structure and Yield Behavior. *Macromolecules* **38,** 10461–10465 (2005).
30. Kristiansen, M. *et al.* The Binary System Isotactic Polypropylene/Bis(3,4-dimethylbenzylidene)sorbitol: Phase Behavior, Nucleation, and Optical Properties. *Macromolecules* **36,** 5150–5156 (2003).
31. Treat, N. D. *et al.* Microstructure formation in molecular and polymer semiconductors assisted by nucleation agents. *Nat. Mater.* **12,** 628–633 (2013).
32. Lindqvist, C. *et al.* Fullerene Nucleating Agents: A Route Towards Thermally Stable Photovoltaic Blends. *Adv. Energy Mater.* DOI: 10.1002/aenm.201301437 (2014). doi:10.1002/aenm.201301437

33. Sharenko, A., Kuik, M., Toney, M. F. & Nguyen, T.-Q. Crystallization-Induced Phase Separation in Solution-Processed Small Molecule Bulk Heterojunction Organic Solar Cells. *Adv. Funct. Mater.* **24,** 3543–3550 (2014).

34. Marco, C., Ellis, G., Gómez, M. A. & Arribas, J. M. Analysis of the isothermal crystallization of isotactic polypropylene nucleated with sorbitol derivatives. *J. Appl. Polym. Sci.* **88,** 2261–2274 (2003).

35. Feng, Y., Jin, X. & Hay, J. N. Effect of nucleating agent addition on crystallization of isotactic polypropylene. *J. Appl. Polym. Sci.* **69,** 2089–2095 (1998).

36. Marco, C., Ellis, G., Gómez, M. A. & Arribas, J. M. Comparative study of the nucleation activity of third-generation sorbitol-based nucleating agents for isotactic polypropylene. *J. Appl. Polym. Sci.* **84,** 2440–2450 (2002).

37. Wunderlich, B. *Macromolecular Physics: Crystal nucleation, growth, annealing*. (Academic Press, 1976).

38. Avrami, M. Kinetics of Phase Change. I General Theory. *J. Chem. Phys.* **7,** 1103–1112 (1939).

39. Avrami, M. Kinetics of Phase Change. II Transformation-Time Relations for Random Distribution of Nuclei. *J. Chem. Phys.* **8,** 212–224 (1940).

40. Avrami, M. Granulation, Phase Change, and Microstructure Kinetics of Phase Change. III. *J. Chem. Phys.* **9,** 177–184 (1941).

41. Hammond, M. R. *et al.* Molecular Order in High-Efficiency Polymer/Fullerene Bulk Heterojunction Solar Cells. *ACS Nano* (2011). doi:doi: 10.1021/nn202951e

42. Love, J. *et al.* Film Morphology of High Efficiency Solution-Processed Small-Molecule Solar Cells. *Adv. Funct. Mater.* **23,** 5019–5026 (2013).

43. Lai, L. F. *et al.* Topological Considerations for the Design of Molecular Donors with Multiple Absorbing Units. *J. Am. Chem. Soc.* **136,** 5591–5594 (2014).

Section II: Investigatoin of the Morphological, Optical and Electronic Properties of a Solution-Processed Small Molecule Bulk Heterojuntion Organic Solar Cell Utilizing a Perylene Diimide Acceptor

A. *Section Introduction*

Solution processed bulk heterojunction organic photovoltaics (BHJ OPVs) have been the subject of significant scientific and industrial research due to their potential as a low cost, scalable source of renewable energy. OPVs have recently surpassed 10% power conversion efficiency (PCE), comparable to what has been achieved with inorganic PV technologies such as amorphous silicon.[1] Additionally, OPVs have demonstrated the ability to be solution processed over large areas[2] and have exhibited extrapolated lifetimes approaching 7 years.[3] Despite these promising advances, many of the donor materials used in high efficiency OPV active layers require multistep synthetic protocols that may hinder their commercial viability.[4] Likewise, fullerene derivatives, ubiquitous in high efficiency BHJ OPVs, are produced via particularly solvent and energy intensive techniques.[5,6] There then exists obvious benefits for using inexpensive, easily mass produced donor materials and fullerene alternatives. To date, however, non-fullerene OPVs significantly underperform fullerene based devices with PCEs of 2-3%.[7–11]

Recently, small molecule donor materials blended with fullerene acceptors have achieved efficiencies approaching those of their polymer counterparts.[12,13] Conjugated small molecules offer several advantages over polymers in that they are monodisperse and can be readily synthesized and purified with standard organic chemistry techniques.[14,15] Thus, combining small molecule donors with non-fullerene acceptors may lead to efficient, scalable OPVs. Despite the potential benefits of a solution processed small molecule:non-fullerene BHJ OPV, there are few examples of such systems.[9,16] Studies of small molecule:non-fullerene BHJ OPVs are therefore necessary to gauge the full potential of BHJ

molecular structural combinations and to develop processing-property-performance relationships for the design and optimization of future non-fullerene OPV systems.

Herein a solution processed BHJ OPV device is fabricated by combining a narrow band gap small molecule donor, p-DTS($FBTTh_2$)$_2$, and a perylene diimide (PDI) acceptor (Figure 15) to achieve a PCE of 3.1%, one of the highest PCEs to date for a BHJ OPV utilizing a non-fullerene acceptor. p-DTS($FBTTh_2$)$_2$ has previously demonstrated utility as a donor molecule in BHJ OPVs, achieving a PCE of 7.0% when combined with phenyl-C_{71}-butyric acid methyl ester ($PC_{71}BM$) as an electron acceptor.[12] PDIs have been investigated as electron acceptors because of their high electron mobility, photochemical stability and strong optical absorption[17,18] and are currently inexpensively produced on the kiloton scale as industrial pigments[19].

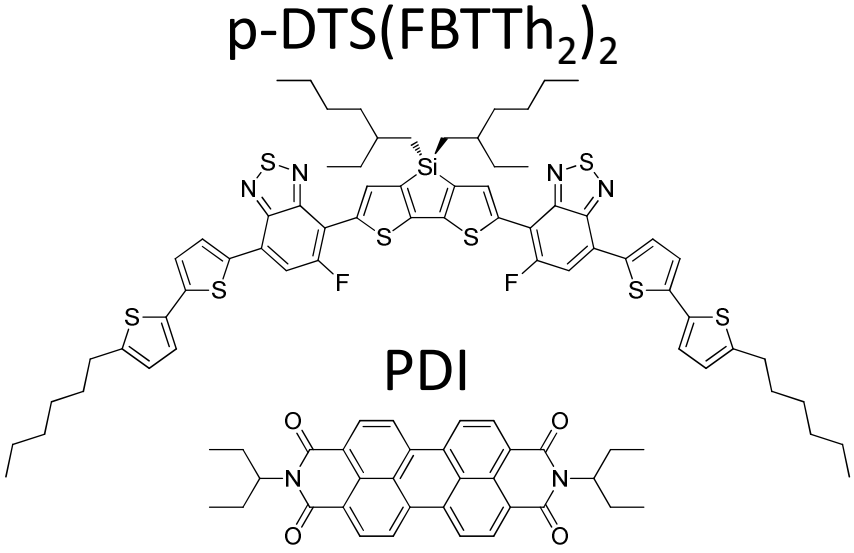

Figure 15: Chemical structures of the electron donor, p-DTS($FBTTh_2$)$_2$, and electron acceptor, PDI, used in this study.

B. The Influence of Solvent Additive on Photovoltaic Performance

Figure 16a displays the current density-voltage (*J-V*) curves of p-DTS(FBTTh$_2$)$_2$:PDI BHJ OPV devices processed from pure chlorobenzene (without DIO) and chlorobenzene with 0.4 vol% 1,8-diiodooctane (with DIO) under simulated AM 1.5 sun illumination. The device processed with DIO exhibits an open-circuit voltage (V_{OC}) of 0.78 V, a J_{SC} of 7.0 mA/cm^2, a fill factor (FF) of 0.57 and a PCE of 3.1%. The device processed without DIO, however, displays very low photovoltaic performance with a V_{OC} of 0.74 V, a J_{SC} of 0.50 mA/cm^2, a FF of 0.35 and a PCE of 0.13%. The external quantum efficiency (EQE) spectra of the blends processed without and with DIO are displayed in Figure 16b. The relative magnitudes of the EQE spectra correlate well to the J_{SC} values determined from the *J-V* curves with the EQE of the device processed with DIO exhibiting a maximum value of approximately 37% while the EQE of the device processed without DIO never exceeds 7%. The use of the solvent additive DIO thus results in a drastic increase in photovoltaic performance due to simultaneous increases in all figures of merit (V_{OC}, J_{SC} and FF). Of note, DIO has previously been shown to increase the PCE of BHJ OPV devices utilizing polymer donors[20] as well as p-DTS(FBTTh$_2$)$_2$:PCBM BHJ OPV devices.[12,21] These changes have largely been correlated to changes in the BHJ morphology.[21,22]

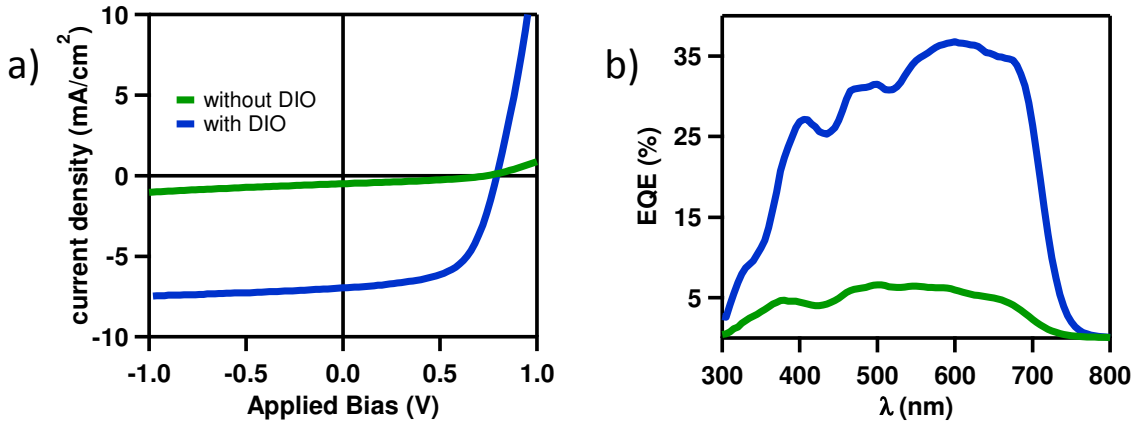

Figure 16: a) *J-V* curves and b) EQE spectra of BHJ OPV devices processed without (green) and with (blue) DIO.

C. *Blend Morphology With and Without Solvent Additive*

In order to understand the drastic difference in photovoltaic performance without and with the solvent additive, the BHJ blend morphology was investigated. 2D GIWAXS images and cake segment cuts are shown in Figure 17. The GIWAXS data of the blend cast without DIO lacks several of the well-defined p-DTS(FBTTh$_2$)$_2$ and PDI peaks exhibited in the GIWAXS data of the blend with DIO indicating the blend with DIO is more structurally ordered than the blend without DIO. The GIWAXS of the blend without DIO, however, appears to contain some peaks partially obscured by peak broadening and/or background amorphous scattering. The presence of these peaks is suggestive that some amount of solid state order exists even in the blend without DIO. As GIWAXS is an x-ray diffraction technique, however, it is only sensitive to crystalline regions of the film capable of satisfying Bragg's condition and is therefore severely biased towards characterization of crystalline order within a film, regardless of the fraction of film containing such order. Alternatively, UV-Vis probes all regions of the film (regardless of solid state order) and the resulting UV-Vis spectrum is therefore representative of the dominant morphological

features in the film.[23] Because of the wealth of information about molecular order associated with UV-Vis data[23], its ability to probe both ordered and disordered regions of a film, and the unambiguous and well established indicators of structural order in the UV-Vis spectra of both p-DTS(FBTTh$_2$)$_2$[12,21] and PDI[24,25], UV-Vis spectroscopy was also used to qualitatively characterize the overall relative structural order in p-DTS(FBTTh$_2$)$_2$:PDI BHJ films cast without and with DIO.

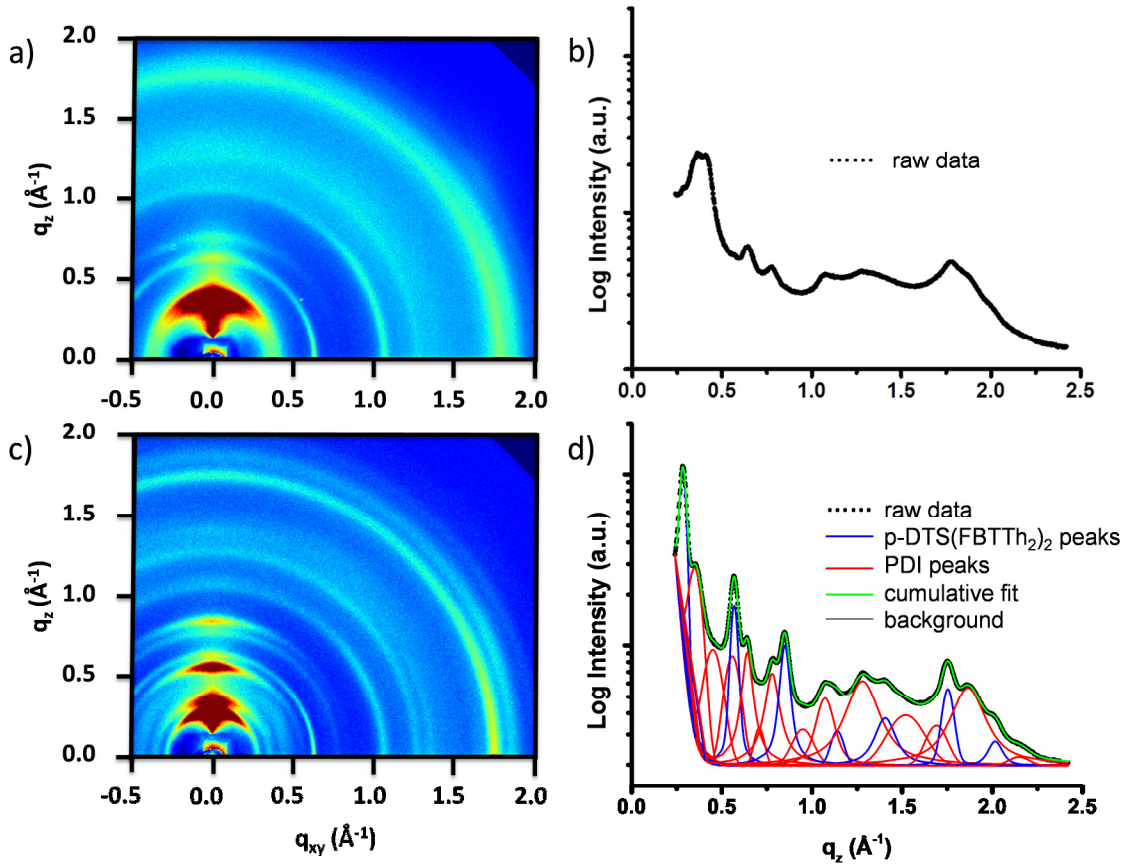

Figure 17 2D GIWAXS images (a, c) and out of plane (chi = 75˚ to 105˚) cake segments (b, d) of p-DTS(FBTTh$_2$)$_2$:PDI BHJ film processed without (a, b) and with (c, d) 0.4 vol. % DIO. p-DTS(FBTTh$_2$)$_2$ and PDI peaks were indexed using their respective single crystal structures as reference.[21,26] Reprinted with permission from Sharenko, A. et al. The Effect of Solvent Additive on Charge Generation and Photovoltaic Performance of a Solution-Processed Small Molecule:Perylene Diimide Bulk Heterojunction Solar Cell. Chem. Mater. (2014). Copyright 2014 American Chemical Society.

The normalized UV-Vis absorption spectra of the blends spin-cast without and with DIO are displayed in Figure 18. These spectra exhibit significant differences. Both spectra display approximately the same number and position of peaks with the major exception being the additional peak at 675 nm observed in the blend processed with DIO compared to the blend processed without DIO. The relative magnitude of the peaks in the two spectra, however, is significantly different. The most intense peaks in the blend processed without DIO are those at 500 and 539 nm, whereas the most intense peaks in the blend processed with DIO are those at 620 and 675 nm. The peak at 675 nm in the blend processed with DIO can be assigned to p-DTS($FBTTh_2$)$_2$ and is present in the pristine molecule's thin film absorption spectra, but absent in its solution spectra. Additionally, the relative intensity of this transition has previously been observed to increase with increasing p-DTS($FBTTh_2$)$_2$ crystallinity.[21] The presence of the p-DTS($FBTTh_2$)$_2$ transition at approximately 675 nm is therefore indicative of p-DTS($FBTTh_2$)$_2$ solid state order, whereas its absence in the blend cast without DIO indicates a relative lack of p-DTS($FBTTh_2$)$_2$ structural order. DIO has previously been shown to have a similar effect on p-DTS($FBTTh_2$)$_2$:phenyl-C_{71}-butyric acid methyl ester ($PC_{71}BM$) BHJ blends in that its use was shown to increase the solid state ordering of p-DTS($FBTTh_2$)$_2$ during spin casting.[27] The peaks at 500 nm and 539 nm in the blend cast without DIO correspond to PDI's 0-1 and 0-0 transition, respectively. It has been shown that PDI crystallization results in a reduction of the intensity of the 0-0 and 0-1 peaks as these transitions are associated with absorption from individual chromophores rather than PDI crystallites.[25,28] The relative decrease in intensity of these peaks upon the addition of DIO to the casting solution is therefore interpreted as indicating that in the blend spin-cast without DIO PDI is predominantly structurally disordered but that DIO directly or indirectly

induces the nucleation of PDI crystallites in the blend spin-cast with DIO. By analyzing the blend UV-Vis spectra cast without and with DIO it can therefore be deduced that the blend film cast without DIO predominantly consists of structurally disordered p-DTS(FBTTh$_2$)$_2$ and PDI molecules, while the addition of DIO results in an increase in the crystallinity of both p-DTS(FBTTh$_2$)$_2$ and PDI. Notably, the increase in both donor and acceptor structural order correlates to a drastic improvement in device photovoltaic performance. It is emphasized that the characterization of the solid state order of the p-DTS(FBTTh$_2$)$_2$:PDI BHJ without and with DIO should be considered on a relative scale as quantifying the absolute order of organic semiconductors is notoriously difficult.[29]

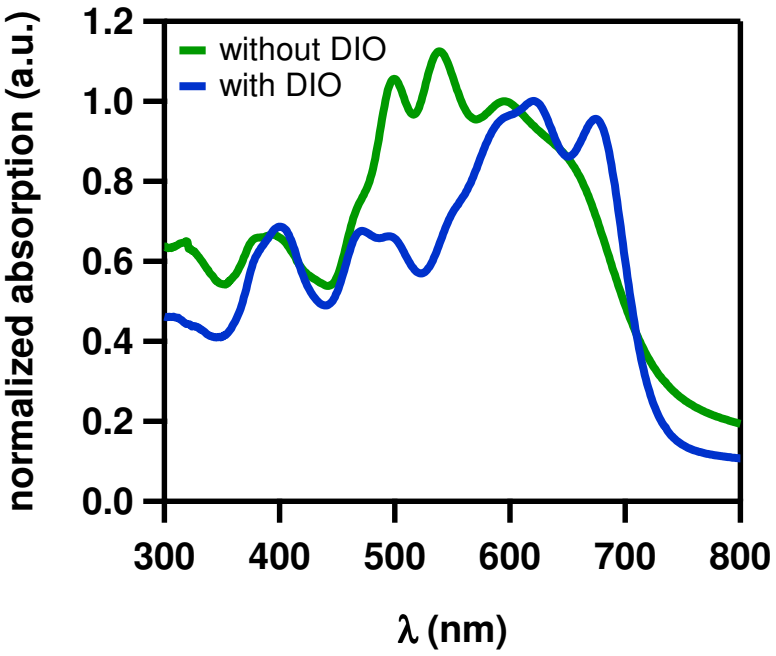

Figure 18 UV-Vis absorption spectra of p-DTS(FBTTh$_2$)$_2$:PDI BHJ films processed without (green) and with (blue) DIO. Reprinted with permission from Sharenko, A. et al. The Effect of Solvent Additive on Charge Generation and Photovoltaic Performance of a Solution-Processed Small Molecule:Perylene Diimide Bulk Heterojunction Solar Cell. Chem. Mater. (2014). Copyright 2014 American Chemical Society.

BHJ blend films were also investigated with atomic force microscopy (AFM) (Figure 19). The root mean square (RMS) roughness of the films increases upon use of DIO, consistent with an increase in the crystallinity of the films.[30] Additionally, the films do not show any sign of large scale phase separation and do not exhibit the micron sized PDI crystallites often observed in other BHJ systems utilizing the PDI donor.[11,31,32] The lack of large PDI crystallites in AFM images is consistent with crystalline correlation length calculations done using the GIWAXS peak fitting in Figure 17d. p-DTS(FBTTh$_2$)$_2$ and PDI peaks were indexed, deconvoluted and fit with pseudo-voigt peak functions using their respective single crystal structures as reference.[21,26] Background scattering was fit using a biexponential function. Using the FWHM of PDI's (200) peak (q_z = 0.35 Å^{-1}), the PDI's CCL was calculated to be 7.4 $\pm$ 3.3 nm. The (001) peak (q_z = 0.28 Å^{-1}) of p-DTS(FBTTh$_2$)$_2$ was used to calculate a CCL of 15.5 $\pm$ 0.3 nm for p-DTS(FBTTh$_2$)$_2$.

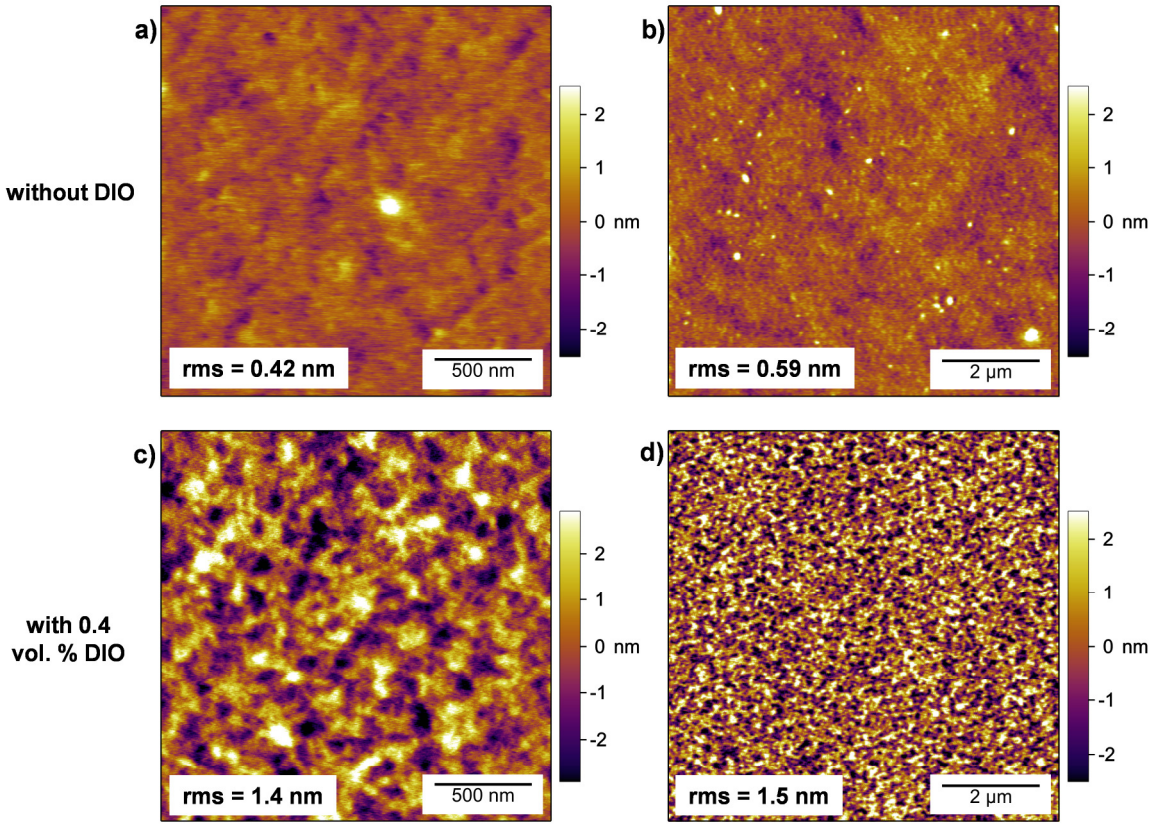

Figure 19 Atomic force microscopy topography images of p-DTS(FBTTh$_2$)$_2$:PDI BHJ blends processed without (a, b) and with (c, d) 0.4 vol. % DIO. Reprinted with permission from Sharenko, A. et al. The Effect of Solvent Additive on Charge Generation and Photovoltaic Performance of a Solution-Processed Small Molecule:Perylene Diimide Bulk Heterojunction Solar Cell. Chem. Mater. (2014). Copyright 2014 American Chemical Society.

D. The Effect of Solvent Additive on Geminate Recombination

In order to investigate the cause of the drastic difference in photovoltaic performance without and with DIO, p-DTS(FBTTh$_2$)$_2$:PDI BHJ blends were probed with transient absorption (TA) spectroscopy in collaboration with the group of Dr. Frédéric Laquai at the Max Planck Institute for Polymer Research. TA pump-probe spectroscopy involves the excitation of a sample with an ultrashort pump laser pulse followed by exposing the sample to an optical supercontinuum probe pulse. Excited states generated by the pump pulse induce a differential absorption that is measured by the probe pulse. The difference in

sample transmission between the excited and non-excited state (ΔT/T) can then be used to infer the population dynamics of the excited states as a function of pump-probe time delay. TA spectroscopy is then uniquely suited to study the charge generation and recombination dynamics of photovoltaic devices.

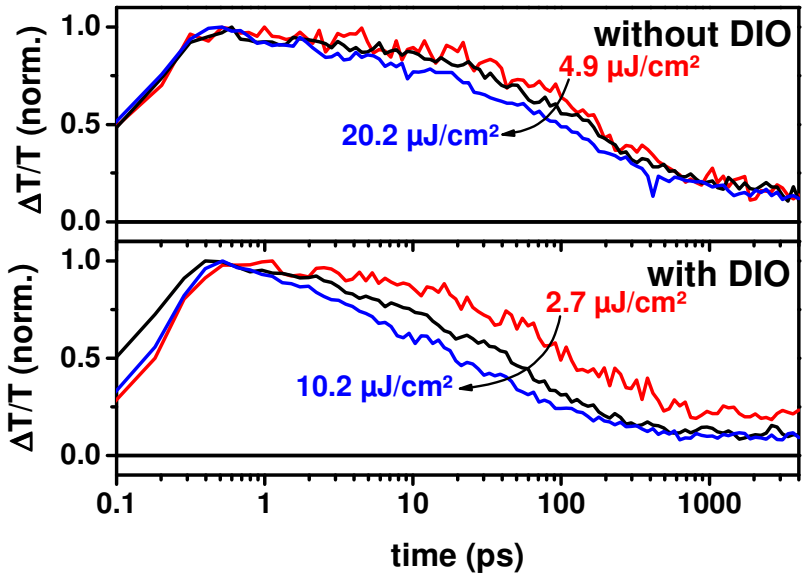

Figure 20 Ground state bleach kinetics of p-DTS(FBTTh$_2$)$_2$:PDI films processed without and with DIO excited at 625 nm. Data collected by Dominik Gehrig. Reprinted with permission from Sharenko, A. et al. The Effect of Solvent Additive on Charge Generation and Photovoltaic Performance of a Solution-Processed Small Molecule:Perylene Diimide Bulk Heterojunction Solar Cell. Chem. Mater. (2014). Copyright 2014 American Chemical Society.

Figure 20 displays the ground state bleach dynamics as a function of excitation intensity. The blend spin-cast without DIO displays only a weak intensity dependence, whereas the blend processed with DIO exhibits a significantly more pronounced intensity dependence indicating geminate recombination dominates in the blend processed without DIO, while non-geminate recombination dominates in the blend processed with DIO. This means that in

the blend without DIO, a negligible amount of free charge carriers are being generated, which likely largely explains the very poor photovoltaic performance of this blend.

The remarkable increase in the efficiency of interfacial charge separation associated with the use of the processing additive DIO in p-DTS($FBTTh_2$)$_2$:PDI films corresponds to a significant increase in the solid state order of both p-DTS($FBTTh_2$)$_2$ and PDI as inferred from UV-Vis measurements. TA spectroscopy has previously been used to observe similar behavior in polymer:PCBM BHJ films. For example, the efficiency of charge generation increases from approximately 68% to 85% upon thermal annealing of poly(3-hexylthiopene):PCBM (P3HT:PCBM) films[33] and in poly[2,6-(4,4-bis-(2-ethylhexyl)-4H-cyclopenta[2,1-b;3,4-b′]-dithiophene)-alt-4,7-(2,1,3-benzothiadiazole)]:PCBM (PCPDTBT:PCBM) films the charge generation efficiency additionally increases upon using the processing additive DIO during film casting.[34] Thermal annealing of P3HT:PCBM films and the use of the processing additive DIO during spin casting of PCPDTBT:PCBM films improves the solid state order of these donor polymers.[22,30] The p-DTS($FBTTh_2$)$_2$:PDI BHJ system differs from these polymer:PCBM BHJ systems, however, as here the use of the processing additive DIO leads to crystallization of both donor and acceptor, which may explain the much more significant increase in the charge separation efficiency between disordered and ordered morphologies compared to previous observations of polymer:PCBM films. In order to gain insight into this observation it is useful to compare the relationship between solid state order and charge generation in p-DTS($FBTTh_2$)$_2$:PDI BHJ OPV devices to p-DTS($FBTTh_2$)$_2$:$PC_{71}BM$ BHJ OPV devices. p-DTS($FBTTh_2$)$_2$:$PC_{71}BM$ BHJ OPV devices cast without DIO form a structurally disordered BHJ morphology lacking significant phase separation, very similar to p-DTS($FBTTh_2$)$_2$:PDI films cast without DIO. However, p-

DTS(FBTTh$_2$)$_2$:PC$_{71}$BM devices processed without DIO exhibit a J_{SC} over 6 mA/cm^2, even though they absorb approximately the same number of photons as optimized p-DTS(FBTTh$_2$)$_2$:PDI BHJ OPV devices.[21,35] Comparing the results reported herein on p-DTS(FBTTh$_2$)$_2$:PDI BHJ OPVs to previous observations on p-DTS(FBTTh$_2$)$_2$:PC$_{71}$BM BHJ OPVs then further supports the suggestion that PDIs require greater solid state order compared to PCBM in order to achieve efficient charge generation.[36] This relationship between solid state order and efficient charge generation may be general for BHJ electron acceptors capable of forming crystalline domains as evidenced by recent work comparing the efficiency of charge generation with the crystallinity of C_{60} and CdS acceptors.[37,38]. It is still unclear, however, specifically why increased solid state order leads to more efficient charge separation in PDI acceptors. Given the delocalization of excited states associated with crystalline molecular semiconductors[39,40] and the crucial role delocalization is thought to play in efficient charge generation at organic heterojunctions,[37,41–43] it is possible that the increased solid state order in p-DTS(FBTTh$_2$)$_2$:PDI films associated with the use of DIO facilitates the delocalization of photogenerated excited states, thereby allowing these states to successfully overcome coulombic forces and produce free charge carriers.

E. Recombination in Optimized Blends

In order to further understand why p-DTS(FBTTh$_2$)$_2$:PDI BHJ OPV devices underperform p-DTS(FBTTh$_2$)$_2$:PCBM BHJ OPV devices the IQE of p-DTS(FBTTh$_2$)$_2$:PDI BHJ OPV devices was determined under different applied voltages and light intensities (Figure 21). Of note, the above TA measurements were performed on blend films without electrodes, essentially in an open-circuit condition, meaning there is no internal electric field to drive generated charge carriers out of the device and then no electrodes to collect the

charges. The following IQE measurements are performed on fully functional OPV devices at short-circuit condition, meaning there is an internal electric field to drive charges out of the device and electrodes to collect said charges.

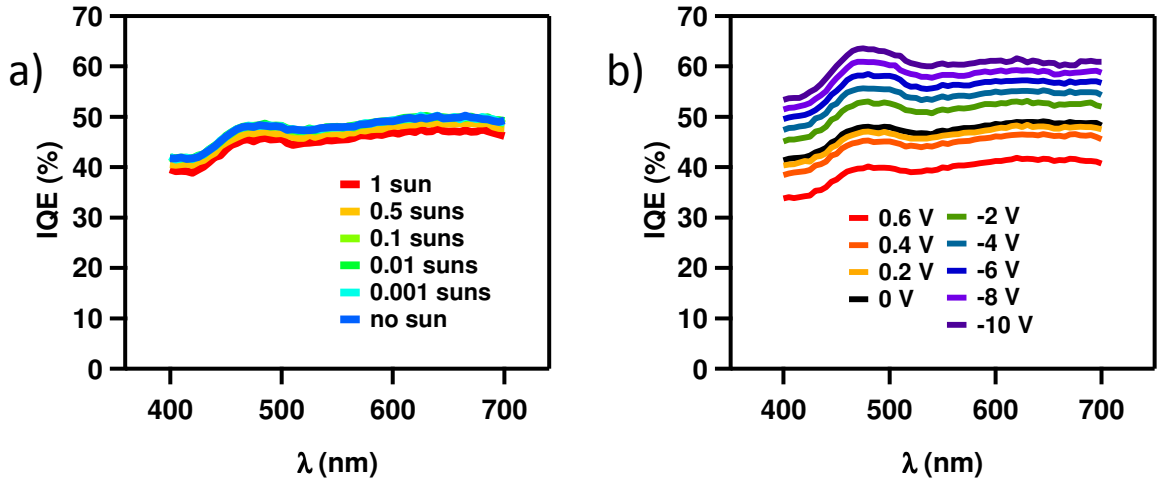

Figure 21 Light intensity dependent (a) and bias dependent (b) IQE of a p-DTS(FBTTh$_2$)$_2$:PDI BHJ solar cell prepared with 0.4 vol% DIO. Light intensity measurements performed at short circuit conditions. Reprinted with permission. © 2014 WILEY-VCH Verlag GmbH & Co. KGaA, Weinheim.

Figure 21a shows the IQE for a p-DTS(FBTTh$_2$)$_2$:PDI BHJ solar cell prepared with DIO to be only ~45%, much reduced compared to the greater than 90% IQE for p-DTS(FBTTh$_2$)$_2$:PCBM devices cast with DIO.[21] The extent to which the low IQE of the p-DTS(FBTTh$_2$)$_2$:PDI device can be attributed to bimolecular recombination was investigated with light intensity dependent IQE as well as hole and electron only diode mobility measurements of p-DTS(FBTTh$_2$)$_2$:PDI blends. The hole and electron mobilities in the solar cell blend were measured to be 7.4 x 10^{-5} and 1.7 x 10^{-4} cm^2 V^{-1} s^{-1} respectively, as determined by fitting the *J-V* characteristics of single carrier diodes to the Mott-Gurney relation for space charge limited current (Figure 22). The electron mobility is one order

lower than what has been reported for fullerene acceptors[44,45]. The reduced electron mobility and relatively low hole mobility therefore likely contribute to the reduced *FF* in this device as compared to p-DTS($FBTTh_2$)$_2$:$PC_{71}BM$ devices.[21,44,46,47] However, it is found that the transport properties are not a limitation to overcoming bimolecular losses at short circuit conditions. As shown in Figure 3a, the difference between the IQE measured at short circuit conditions with 1 sun white light background and no white light background is only approximately 3%. IQE measurements performed with background illumination less than 0.1 suns converge to the same value as without any background illumination. It is then estimated that only approximately 3% of absorbed photons are lost to bimolecular recombination at short circuit conditions.[48,49] These findings therefore suggest that while the *FF* may be transport limited, bimolecular recombination is only a small fraction of the total recombination losses at short circuit. The modest increase in IQE under strong reverse bias exhibited in Figure 21b may be due to a field dependent charge generation mechanism,[50,51] or the release of trapped charge carriers as the negative bias increases the internal electric field within the device. More notable however, is that even at -10 V the IQE is still only ~60% suggesting that in addition to a voltage dependent loss mechanism, there are significant losses that are likely independent of voltage.

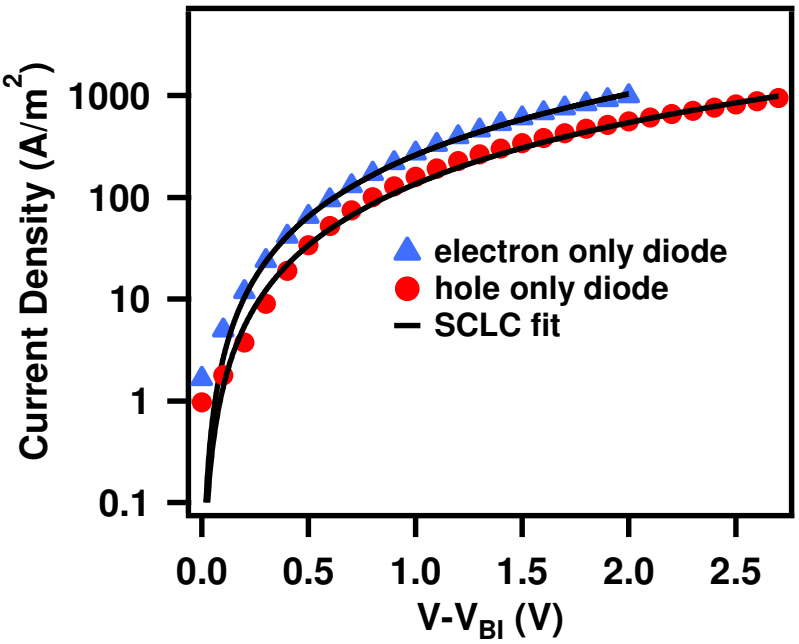

Figure 22 *J-V* characteristics of electron and hole only devices of p-DTS(FBTTh$_2$)$_2$:PDI blends. In both cases films were 120 nm thick. Solubility limitations excluded the possibility of making thicker films in order to verify these mobility values were consistent over a range of film thicknesses. Reprinted with permission. © 2014 WILEY-VCH Verlag GmbH & Co. KGaA, Weinheim.

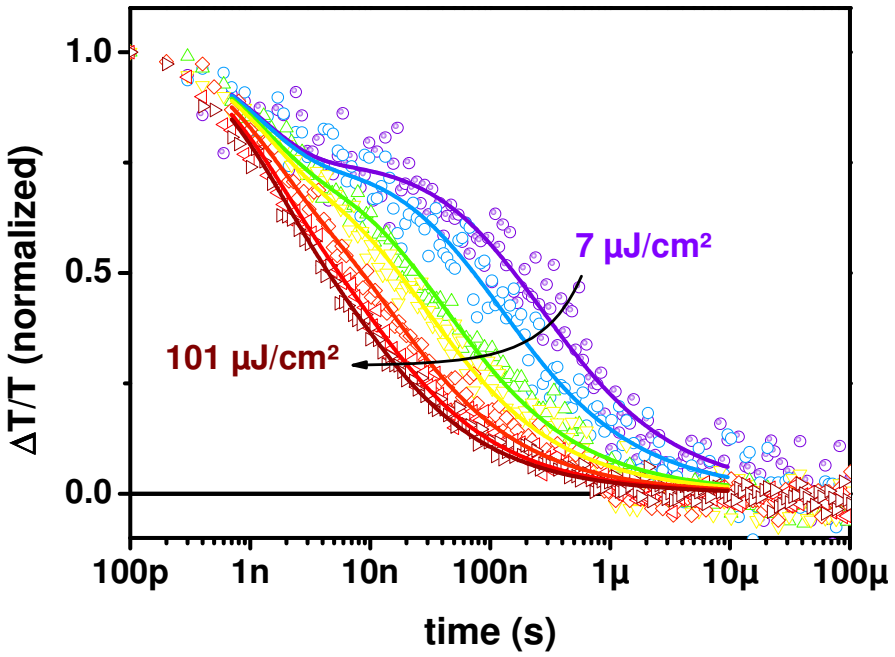

Figure 23 Excitation intensity dependence of the PIA dynamics (symbols) and respective fits (lines) using the recombination model detailed elsewhere.[33] Data collected by Dominik

Gehrig. Reprinted with permission from Sharenko, A. et al. The Effect of Solvent Additive on Charge Generation and Photovoltaic Performance of a Solution-Processed Small Molecule:Perylene Diimide Bulk Heterojunction Solar Cell. Chem. Mater. (2014). Copyright 2014 American Chemical Society.

Figure 23 shows long delay TA data fit with a recombination model introduced by Howard et al. The model assumes concomitant recombination of CT states via a monomolecular and geminate recombination process parallel to recombination of free charges via a non-geminate recombination process.[33] In the present case, this model concludes that approximately 76% of the charges surviving the first ns are free charge carriers as opposed to bound CT states. This then means that there is still a significant amount of geminate recombination in optimized p-DTS($FBTTh_2$)$_2$:PDI BHJ OPV devices as not all bound CT states are able to form spatially separated free charges. This results is consistent with the bias dependent IQE measurements above which seemingly plateaued at ~60% at -10 V. Some of the remaining ~40% losses can then likely be attributed to geminate losses such as the recombination of CT states rather than the formation of free charge carriers.

It is difficult to determine what exactly prevents the remaining CT states from dissociating into free charge carriers in p-DTS($FBTTh_2$)$_2$:PDI films processed with DIO. Perhaps additional increases in the solid state order of p-DTS($FBTTh_2$)$_2$ and/or the PDI would result in more efficient charge generation, provided this could be achieved without leading to phase separation on a length scale larger than the exciton diffusion length. PDIs, however, may lack some fundamental property fullerene derivatives possess that enables extremely efficient charge generation.[52] More work is needed to better understand the charge

generation process, especially in systems utilizing non-fullerene acceptors, before these questions can be answered.

F. Section Conclusion

It has been demonstrated that using the processing additive DIO during spin-casting of p-DTS($FBTTh_2$)$_2$:PDI BHJ OPV devices leads to a drastic improvement in PCE compared to devices processed without the additive, increasing the PCE from 0.13% to 3.1%. Using UV-Vis absorption spectroscopy and GIWAXS it has been shown that the increased PCE is associated with a significant increase in both p-DTS($FBTTh_2$)$_2$ and PDI solid state order. TA spectroscopy measurements are used to characterize the charge generation and recombination dynamics of p-DTS($FBTTh_2$)$_2$:PDI films processed without and with DIO. Fast, intensity independent geminate recombination was found to be the dominant loss process in blends spin-cast without DIO, while geminate recombination was significantly reduced in blends cast with DIO, thereby increasing the yield of free charge carriers in these blends as demonstrated by the occurrence of intensity dependent non-geminate recombination in their charge carrier dynamics. Devices processed without DIO are therefore relatively structurally disordered compared to the blend processed with DIO and display negligible photovoltaic efficiency because the vast majority of excitons form interfacial CT states that recombine prior to dissociation. In contrast, in blends processed with DIO both p-DTS($FBTTh_2$)$_2$ and PDI exhibit increased structural order as well as phase separation and a much higher PCE, largely due to a drastic increase of the efficiency with which excitons dissociate into free charge carriers. This section thus provide useful insight into the conditions under which photogenerated excitons are able to overcome coulombic forces to produce spatially-separated free charge carriers in a BHJ architecture when using a

non-fullerene acceptor. Light intensity dependent IQE measurements suggest that bimolecular recombination is not a significant loss process in p-DTS($FBTTh_2$)$_2$:PDI devices cast with DIO at short-circuit condition, however, the relatively low hole and electron mobilities of this device may limit the FF. The blend processed with DIO additionally displays a significant amount of geminate recombination of coulombically-bound CT states that do not form free charge carriers as determined from bias dependent IQE as well as long delay TA measurements. This relatively low efficiency of charge separation compared to fullerene acceptors largely explains why p-DTS($FBTTh_2$)$_2$:PDI devices exhibit less efficient photovoltaic performance compared to p-DTS($FBTTh_2$)$_2$:PCBM devices, which exhibit a PCE of 7.0% and an IQE exceeding 90%.[21] It remains unclear, however, why the use of the PDI as an electron acceptor leads to less efficient charge generation compared to the use of PCBM as an electron acceptor. Accordingly, it is emphasized that further advances in the fabrication of high efficiency BHJ OPV devices utilizing PDI acceptors are dependent on developing a more thorough understanding of the relationship between PDI chemical structure, BHJ processing conditions, thin film morphology and the fundamental processes associated with charge generation in in these devices.

G. References

1. Green, M. A., Emery, K., Hishikawa, Y., Warta, W. & Dunlop, E. D. Solar cell efficiency tables (version 39). *Prog. Photovolt. Res. Appl.* **20,** 12–20 (2012).
2. Krebs, F. C., Gevorgyan, S. A. & Alstrup, J. A roll-to-roll process to flexible polymer solar cells: model studies, manufacture and operational stability studies. *J. Mater. Chem.* **19,** 5442–5451 (2009).

3. Peters, C. H. *et al.* High Efficiency Polymer Solar Cells with Long Operating Lifetimes. *Adv. Energy Mater.* **1,** 491–494 (2011).
4. Osedach, T. P., Andrew, T. L. & Bulović, V. Effect of synthetic accessibility on the commercial viability of organic photovoltaics. *Energy Environ. Sci.* **6,** 711–718 (2013).
5. Anctil, A., Babbitt, C. W., Raffaelle, R. P. & Landi, B. J. Material and Energy Intensity of Fullerene Production. *Environ. Sci. Technol.* **45,** 2353–2359 (2011).
6. Anctil, A., Babbitt, C., Landi, B. & Raffaelle, R. P. Life-cycle assessment of organic solar cell technologies. in *2010 35th IEEE Photovolt. Spec. Conf. PVSC* 000742–000747 (IEEE, 2010). doi:10.1109/PVSC.2010.5617085
7. Sharma, G. D., Roy, M. S., Mikroyannidis, J. A. & Justin Thomas, K. R. Synthesis and characterization of a new perylene bisimide (PBI) derivative and its application as electron acceptor for bulk heterojunction polymer solar cells. *Org. Electron.* **13,** 3118–3129 (2012).
8. Bloking, J. T. *et al.* Solution-Processed Organic Solar Cells with Power Conversion Efficiencies of 2.5% using Benzothiadiazole/Imide-Based Acceptors. *Chem Mater* **23,** 5484–5490 (2011).
9. Holcombe, T. W. *et al.* Steric Control of the Donor/Acceptor Interface: Implications in Organic Photovoltaic Charge Generation. *J. Am. Chem. Soc.* **133,** 12106–12114 (2011).
10. Lin, Y., Li, Y. & Zhan, X. A Solution-Processable Electron Acceptor Based on Dibenzosilole and Diketopyrrolopyrrole for Organic Solar Cells. *Adv. Energy Mater.* DOI: 10.1002/aenm.201200911 (2013). doi:10.1002/aenm.201200911

11. Rajaram, S., Shivanna, R., Kandappa, S. K. & Narayan, K. S. Nonplanar Perylene Diimides as Potential Alternatives to Fullerenes in Organic Solar Cells. *J. Phys. Chem. Lett.* **3,** 2405–2408 (2012).
12. Van der Poll, T. S., Love, J. A., Nguyen, T.-Q. & Bazan, G. C. Non-Basic High-Performance Molecules for Solution-Processed Organic Solar Cells. *Adv. Mater.* **24,** 3646–3649 (2012).
13. Zhou, J. *et al.* Small Molecules Based on Benzo[1,2-b:4,5-b′]dithiophene Unit for High-Performance Solution-Processed Organic Solar Cells. *J. Am. Chem. Soc.* **134,** 16345–16351 (2012).
14. Walker, B., Kim, C. & Nguyen, T.-Q. Small Molecule Solution-Processed Bulk Heterojunction Solar Cells†. *Chem Mater* **23,** 470–482 (2010).
15. Mishra, A. & Bäuerle, P. Small Molecule Organic Semiconductors on the Move: Promises for Future Solar Energy Technology. *Angew. Chem. Int. Ed.* **51,** 2020–2067 (2012).
16. Walker, B., Han, X., Kim, C., Sellinger, A. & Nguyen, T.-Q. Solution-Processed Organic Solar Cells from Dye Molecules: An Investigation of Diketopyrrolopyrrole:Vinazene Heterojunctions. *ACS Appl Mater Interfaces* **4,** 244–250 (2011).
17. Li, C. & Wonneberger, H. Perylene Imides for Organic Photovoltaics: Yesterday, Today, and Tomorrow. *Adv. Mater.* **24,** 613–636 (2012).
18. Huang, C., Barlow, S. & Marder, S. R. Perylene-3,4,9,10-tetracarboxylic Acid Diimides: Synthesis, Physical Properties, and Use in Organic Electronics. *J. Org. Chem.* **76,** 2386–2407 (2011).

19. Smith, H. M. *High Performance Pigments*. (Wiley-VCH Verlag-GmbH, 2002).
20. Peet, J. *et al.* Efficiency enhancement in low-bandgap polymer solar cells by processing with alkane dithiols. *Nat. Mater.* **6,** 497–500 (2007).
21. Love, J. *et al.* Film Morphology of High Efficiency Solution-Processed Small-Molecule Solar Cells. *Adv. Funct. Mater.* **23,** 5019–5026 (2013).
22. Rogers, J. T., Schmidt, K., Toney, M. F., Kramer, E. J. & Bazan, G. C. Structural Order in Bulk Heterojunction Films Prepared with Solvent Additives. *Adv. Mater.* **23,** 2284–2288 (2011).
23. Salleo, A., Kline, R. J., DeLongchamp, D. M. & Chabinyc, M. L. Microstructural Characterization and Charge Transport in Thin Films of Conjugated Polymers. *Adv. Mater.* **22,** 3812–3838 (2010).
24. Würthner, F. Perylene bisimide dyes as versatile building blocks for functional supramolecular architectures. *Chem. Commun.* 1564–1579 (2004). doi:10.1039/B401630K
25. Balakrishnan, K. *et al.* Nanobelt Self-Assembly from an Organic n-Type Semiconductor: Propoxyethyl-PTCDI. *J. Am. Chem. Soc.* **127,** 10496–10497 (2005).
26. Maniukiewicz, W., Bojarska, J., Olczak, A., Dobruchowska, E. & Wiatrowski, M. 2,9-Di-3-pentylanthra[1,9-def:6,5,10- d'e'f']diisoquinoline-1,3,8,10-tetrone. *Acta Crystallogr.* **66,** o2570–o2571 (2010).
27. Perez, L. A. *et al.* Solvent Additive Effects on Small Molecule Crystallization in Bulk Heterojunction Solar Cells Probed During Spin Casting. *Adv. Mater.* **25,** 6380–6384 (2013).

28. Keivanidis, P. E., Howard, I. A. & Friend, R. H. Intermolecular Interactions of Perylene diimides in Photovoltaic Blends of Fluorene Copolymers: Disorder Effects on Photophysical Properties, Film Morphology and Device Efficiency. *Adv. Funct. Mater.* **18,** 3189–3202 (2008).
29. Rivnay, J., Mannsfeld, S. C. B., Miller, C. E., Salleo, A. & Toney, M. F. Quantitative Determination of Organic Semiconductor Microstructure from the Molecular to Device Scale. *Chem. Rev.* **112,** 5488–5519 (2012).
30. Verploegen, E. *et al.* Effects of Thermal Annealing Upon the Morphology of Polymer–Fullerene Blends. *Adv. Funct. Mater.* **20,** 3519–3529 (2010).
31. Ye, T., Singh, R., Butt, H.-J., Floudas, G. & Keivanidis, P. E. Effect of Local and Global Structural Order on the Performance of Perylene Diimide Excimeric Solar Cells. *ACS Appl. Mater. Interfaces* **5,** 11844–11857 (2013).
32. Li, J., Dierschke, F., Wu, J., Grimsdale, A. C. & Müllen, K. Poly(2,7-carbazole) and perylene tetracarboxydiimide: a promising donor/acceptor pair for polymer solar cells. *J. Mater. Chem.* **16,** 96–100 (2006).
33. Howard, I. A., Mauer, R., Meister, M. & Laquai, F. Effect of Morphology on Ultrafast Free Carrier Generation in Polythiophene:Fullerene Organic Solar Cells. *J. Am. Chem. Soc.* **132,** 14866–14876 (2010).
34. Etzold, F. *et al.* The Effect of Solvent Additives on Morphology and Excited-State Dynamics in PCPDTBT:PCBM Photovoltaic Blends. *J. Am. Chem. Soc.* **134,** 10569–10583 (2012).
35. Sharenko, A. *et al.* A High-Performing Solution-Processed Small Molecule:Perylene Diimide Bulk Heterojunction Solar Cell. *Adv. Mater.* **25,** 4403–4406 (2013).

36. Pensack, R. D., Guo, C., Vakhshouri, K., Gomez, E. D. & Asbury, J. B. Influence of Acceptor Structure on Barriers to Charge Separation in Organic Photovoltaic Materials. *J Phys Chem C* **116,** 4824–4831 (2012).
37. Bernardo, B. *et al.* Delocalization and dielectric screening of charge transfer states in organic photovoltaic cells. *Nat. Commun.* **5,** (2014).
38. Bansal, N. *et al.* Influence of Crystallinity and Energetics on Charge Separation in Polymer–Inorganic Nanocomposite Films for Solar Cells. *Sci. Rep.* **3,** (2013).
39. Haskal, E. I., Shen, Z., Burrows, P. E. & Forrest, S. R. Excitons and exciton confinement in crystalline organic thin films grown by organic molecular-beam deposition. *Phys. Rev. B* **51,** 4449–4462 (1995).
40. Shen, Z. & Forrest, S. R. Quantum size effects of charge-transfer excitonsin nonpolar molecular organic thin films. *Phys. Rev. B* **55,** 10578–10592 (1997).
41. Bakulin, A. A. *et al.* The Role of Driving Energy and Delocalized States for Charge Separation in Organic Semiconductors. *Science* **335,** 1340–1344 (2012).
42. Jailaubekov, A. E. *et al.* Hot charge-transfer excitons set the time limit for charge separation at donor/acceptor interfaces in organic photovoltaics. *Nat. Mater.* **12,** 66–73 (2013).
43. Vandewal, K. *et al.* Efficient charge generation by relaxed charge-transfer states at organic interfaces. *Nat. Mater.* **13,** 63–68 (2014).
44. Proctor, C. M., Kim, C., Neher, D. & Nguyen, T.-Q. Nongeminate Recombination and Charge Transport Limitations in Diketopyrrolopyrrole-Based Solution-Processed Small Molecule Solar Cells. *Adv. Funct. Mater.* **23,** 3584–3594 (2013).

45. Mihailetchi, V. d. *et al.* Electron Transport in a Methanofullerene. *Adv. Funct. Mater.* **13,** 43–46 (2003).

46. Baumann, A., Lorrmann, J., Rauh, D., Deibel, C. & Dyakonov, V. A New Approach for Probing the Mobility and Lifetime of Photogenerated Charge Carriers in Organic Solar Cells Under Real Operating Conditions. *Adv. Mater.* **24,** 4381–4386 (2012).

47. Wagenpfahl, A., Deibel, C. & Dyakonov, V. Organic Solar Cell Efficiencies Under the Aspect of Reduced Surface Recombination Velocities. *IEEE J. Sel. Top. Quantum Electron.* **16,** 1759–1763 (2010).

48. Bartelt, J. A. *et al.* The Importance of Fullerene Percolation in the Mixed Regions of Polymer–Fullerene Bulk Heterojunction Solar Cells. *Adv. Energy Mater.* **3,** 364–374 (2012).

49. Wehenkel, D. J., Hendriks, K. H., Wienk, M. M. & Janssen, R. A. J. The effect of bias light on the spectral responsivity of organic solar cells. *Org. Electron.* **13,** 3284–3290 (2012).

50. Albrecht, S. *et al.* On the Field Dependence of Free Charge Carrier Generation and Recombination in Blends of PCPDTBT/PC70BM: Influence of Solvent Additives. *J. Phys. Chem. Lett.* **3,** 640–645 (2012).

51. Kniepert, J., Schubert, M., Blakesley, J. C. & Neher, D. Photogeneration and Recombination in P3HT/PCBM Solar Cells Probed by Time-Delayed Collection Field Experiments. *J. Phys. Chem. Lett.* **2,** 700–705 (2011).

52. Liu, T. & Troisi, A. What Makes Fullerene Acceptors Special as Electron Acceptors in Organic Solar Cells and How to Replace Them. *Adv. Mater.* **25,** 1038–1041 (2013).

Appendix- GIWAXS Data Processing Using WXDiff Software Package

All GIWAXS measurements in this dissertation were performed at Stanford Synchrotron Radiation Lightsource beamline 11-3 using a photon energy of 12.7 keV with a sample to detector distance of approximately 400 mm. Experiments were performed under a helium environment to minimize background scattering and sample damage from the x-ray beam. An incident angle of 0.12˚ (above the critical angle of the BHJ blend, but below the critical angle of the substrate to ensure probing of the BHJ blend and not the substrate) was used in all cases. Images were collected with a MAR-345 2D image plate. A custom built heating stage was utilized as described elsewhere for in-situ heating measurements.[1] The absolute temperature values during these experiments are estimated to have an error of ± 3 ˚C. This is largely the result of temperature fluctuations as a function of position on the film as well as over time. For all GIWAXS measurements samples were spin-cast onto silicon substrates previously coated with PEDOT:PSS to mimic a solar cell architecture. Silicon substrates were used so as to reduce background scattering from the substrate.

2D diffraction images were processed with the software package WxDiff, provided by SSRL scientist Dr. Stefan Mannsfeld. This processing involved the isolation of specific peaks, background subtraction and conversion of 2D data to 1D data that could be fit with a pseudo-Voigt function in OriginPro 8.6. This process is further explained below.

A 2D image is loaded in WXDiff and a specific peak is isolated using the "CakeSeg" functionality:

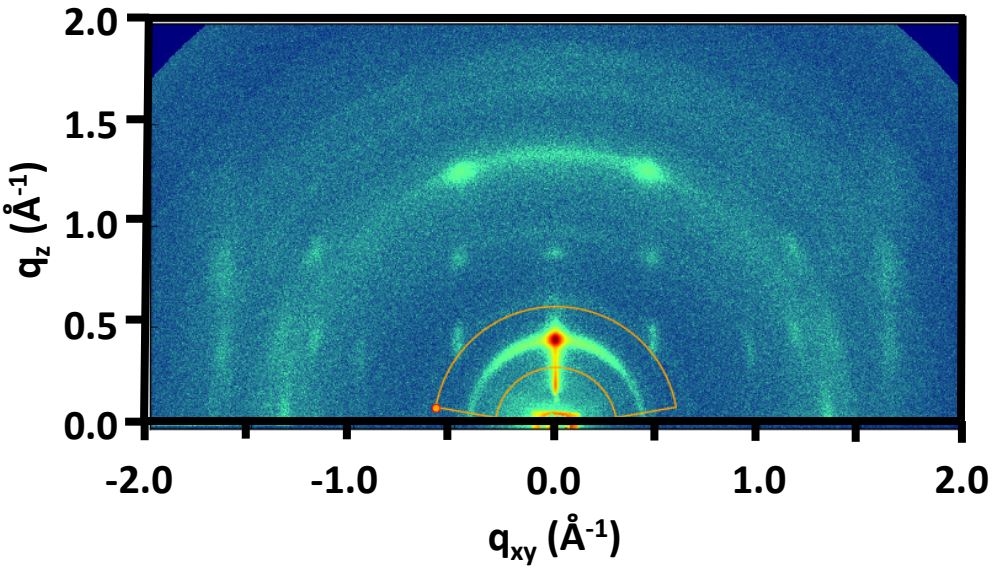

Figure A1 2D GIWAXS image of DPP(TBFu)$_2$ thin film measured in-situ above it's T_{CC}. The (100) peak is enclosed in a cake segment for further analysis (orange region). Imaged copied from WXDiff software.

The 2D data enclosed in the cake segment is then converted to a plot of chi (polar angel) vs. q. The "peak" functionality is then used to define the region of interest (white rectangle) and the background (orange shaded regions):

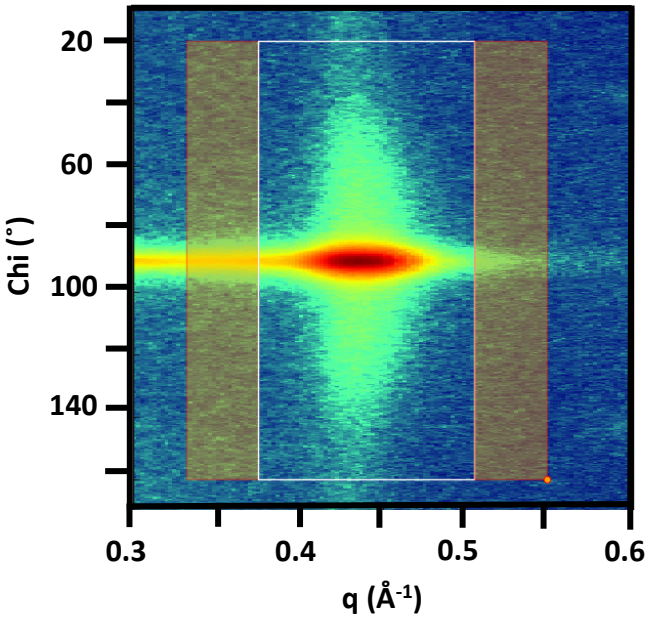

Figure A2 The cake segment in Figure A1 has been converted to a plot of chi (polar angle) vs. q. The enclosed area around the (100) peak indicates the region used for summation of peak intensity. Background was subtracted by fitting the intensity in the shaded orange regions to a polynomial in order to determine precise boundary conditions. These boundary conditions were then extended into the peak area. Imaged copied from WXDiff software.

A peak column sum is then performed to produce a plot of intensity vs. q:

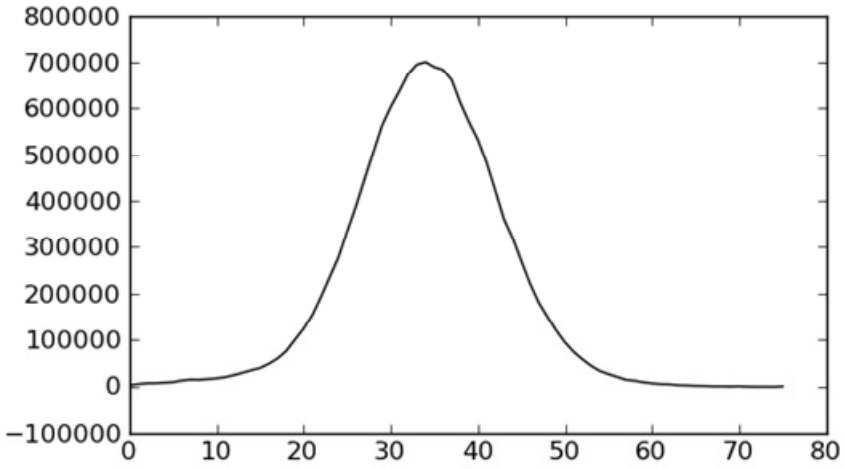

Figure A3 Plot of intensity vs. q (displayed as pixels but exportable as q) produced by performing a "Peak: col sum" of Figure 2A. Imaged copied from WXDiff software.

The data in Figure A3 is then exported to OriginPro 8.6 and fit with a pseudo-Voigt function. A pseudo-Voigt function is used because this linear combination of a Lorentzian and a Gaussian most accurately captures peak broadening from paracrystalline disorder and lattice-parameter fluctuation in organic semiconductors.[2]

References

1. Verploegen, E. *et al.* Effects of Thermal Annealing Upon the Morphology of Polymer–Fullerene Blends. *Adv. Funct. Mater.* **20,** 3519–3529 (2010).
2. Rivnay, J., Noriega, R., Kline, R. J., Salleo, A. & Toney, M. F. Quantitative analysis of lattice disorder and crystallite size in organic semiconductor thin films. *Phys. Rev. B* **84,** 045203 (2011).